ABSTRACT

Title of Thesis: IMPROVING INVERSE ANALYSIS OF PYROLYSIS MODEL PARAMETERIZATION USING HILL CLIMBING ALGORITHMS

Gregory Joseph Fiola, Master of Science, 2019

Thesis Directed By: Dr. Stanislav Stoliarov, Associate Professor, Department of Fire Protection Engineering

Pyrolysis models are valuable tools for understanding material flammability and modeling fire growth. However, the development of comprehensive pyrolysis models is difficult and time-consuming due to the sheer number of material parameters required. Previous parameterization attempts employ massively parallel optimization problems using heuristic search algorithms to extract parameters from experimental data, but have been criticized for lacking physical significance and having reduced

accuracy outside of calibrated ranges. This work sought to improve upon a previously developed manual methodology wherein the experimental results of both milligram- and bench-scale tests are inversely analyzed in a hierarchical approach. Three steps in the hierarchical process are automated using simple steepest ascent hill climbing optimization algorithms. The novelty of this approach lies in the custom fitness criteria and highly constrained and physical significant search space resulting from well-defined experiments. Two distinct materials were studied to evaluate the methodology: poly(methyl methacrylate) and rigid polyisocyanurate foam. The optimization programs were able to consistently fit both mass loss rate (MLR) from thermogravimetry (TGA) experiments and back surface temperature histories from Controlled Atmosphere Gasification Apparatus (CAPA II) experiments within experimental uncertainty. Models were validated against independent MLR histories from CAPA II experiments under low and high heat fluxes.

IMPROVING INVERSE ANALYSIS OF PYROLYSIS MODEL PARAMETERIZATION USING HILL CLIMBING ALGORITHMS

by

Gregory Joseph Fiola

Thesis submitted to the Faculty of the Graduate School of the
University of Maryland, College Park, in partial fulfillment
of the requirements for the degree of
Master of Science
2019

Advisory Committee:
Professor Stanislav Stoliarov, Ph.D., Chair
Professor Arnaud Trouvé
Professor Michael Gollner

Acknowledgements

Dr. Stanislav Stoliarov deserves the highest thanks and acknowledgement for his provisions of insight, instruction, and guidance throughout this study. Thank you for redefining my standards of work quality. I see it as a great privilege to have worked with someone of your expertise, who is willing to offer great knowledge with great patience. Thank you immensely for this opportunity.

I would like to thank and acknowledge my committee members, Dr. Arnaud Trouvé and Dr. Michael Gollner, who have generously given their time to review this work. Thank you for your teaching and instruction over the past 4 years. It is an honor to have your participation on this committee.

My research group has made the office and labs more than just a place for research – thank you all for creating an engaging and enjoyable environment. Dushyant, thank you for being 'Mr. Everything' for the invaluable teaching and intuition on, well, everything. Thank you for sharing some of your expertise and being a good friend at the same time. Josh and Conor, thank you for answering to my relentless questions. Jacques, Yan, Ahmed, and the rest of the group; thank you for the camaraderie throughout this research journey we've embarked on together.

I would like to extend the utmost thanks to my parents and sister, Jaclyn, for their unwavering love and support. They have demonstrated to me the value of education, a love for learning, and a hard work ethic in their own paths, and are the greatest inspiration. Thank you for believing in me, for the compliments and criticisms, for being my foundation, and sharpening me into who I am today.

Lastly, I would like to acknowledge the Federal Aviation Administration (grant #16-G-017) and the grant monitor, Dr. Richard E. Lyon, for the generous financial supported which made this work possible.

Table of Contents

List of Tables

List of Figures

Chapter 1: Introduction

1.1 Background and Motivation

A major bottleneck in the current state of the art of computational fire modeling is the ability to accurately calculate the rate of gaseous fuel production from condensed phase materials. Accurately predicting transient rates of gasification is essential to predicating fire spread phenomena such as ignition and spread rates. The process of thermally degrading a condensed phase material to produce volatilized gasses, namely pyrolysis, involves complex mechanisms that are a growing topic of study in the field of fire research and material science. Recent advancements in pyrolysis modeling has evolved from the less complex thermal models to comprehensive models amid the development of several open source numerical pyrolysis solvers, namely Gpyro [1], ThermaKin [2], and the condensed phase sub model in the Fire Dynamics Simulator (FDS) [3]. These numerical solvers were all developed independently, but are built upon highly similar governing equations and mathematical formulations, with the only differences arising in the implementations of submodels [4]. Comprehensive pyrolysis models employ a set of governing equations that account for the kinetic decomposition scheme coupled with heat and mass conservation statements to represent the chemical and physical changes occurring during pyrolysis. Many of these processes are highly complicated and intertwined. Therefore, modeling has been said to be a "compromise between simplification of physical phenomena and the ability to consider as many details as possible" [5]. One substantial detail to consider in this problem is the material property dataset provided to the model.

A comprehensive pyrolysis model requires a large set of material properties to make accurate predictions, including kinetics and thermodynamics of decomposition, heats of

combustion of gaseous products, optical properties, and heat and mass transport properties of condensed-phase components during thermal degradation. A full parameterization such as this requires a complete set of properties specific to the material at hand, which account for changes and transience associated with chemical, optical, and physical changes during pyrolysis and changes in temperature. This task is both difficult and time consuming due to the sheer number of parameters required. For some materials, a complete set of material properties can be found in literature, but variation can arise between similar materials from different manufacturers [6,7], and a convenient database of peer-reviewed properties is not currently available [8]. Therefore, several methodologies have arisen to undertake the model parameterization process.

Modern comprehensive pyrolysis models are typically parameterized by means of inverse modeling experimental data. Several techniques to solve these inverse problems exist, ranging from "massively parallel automated search methodologies" to manual methodologies [4]. While in many contexts within the fire modeling community, 'optimization' refers simply to any means of solving the multi-variable problem of inverse modeling, this study will refer to 'optimization' as a practice involving automated search algorithms to distinguish the approach from automation-free manual methodologies.

The automated parallel optimization methodology employs the use of a variety of optimization techniques and algorithms (including evolutionary algorithms (EAs) such as genetic algorithms (GA), Shuffled Complex Evolution (SCE), and Stochastic Hill Climber (SHC)) in an attempt to concurrently generate a complete parameter set that accurately reproduces a set of experimental data, typically mass loss rate (MLR) data from bench scale tests such as a cone calorimeter (ASTM E1354 [9]) or Fire Propagation Apparatus (FPA) (ASTM E2058 [10]). Bulk optimization such as this sometimes requires up to 100,000 iterations to converge on a solution, depending on the efficiency of the algorithm and the size

of its search space [4]. This methodology benefits from speed and efficiency, and is not very labor intensive. While this method is capable of producing accurate predictions of the training data, critics of this bulk optimization methodology point out that resultant ‘effective values’ (or ‘equivalent values’) are not always physically meaningful due to compensation effects between parameters. Accordingly, the validity of model predictions beyond the calibrated domain has been questioned [11].

A manual inverse modeling approach aims to determine parameters using a combination of direct measurements and inverse analysis from a hierarchical set of well-defined milligram-scale and bench scale experiments. Milligram scale experiments, such as Thermogravimetric Analysis (TGA) and Differential Scanning Calorimetry (DSC), test thermally thin samples which eliminate the influence of heat and mass transport within the samples to allow for determination of the isolated kinetics and thermodynamics of decomposition, respectively. The resulting inverse analysis problems are constrained tightly enough to be solved in a feasible number of manual inverse guesses. Subsequent bench scale tests reintroduce heat and mass transfer variables for inverse analysis of thermal transport properties. Using the constraints from milligram-scale analysis, this problem can also be solved in a reasonable number of manually iterative steps. Proponents of this methodology argue that results are more accurate and meaningful [12]. However, this manual iterative process is quite labor intensive and time consuming, and requires costly specialized laboratory equipment which is not practically available to all researchers.

The present study seeks to improve upon an existing model development methodology by combining desirable aspects of both the manual and automated optimization techniques. A previously established manual parameterization methodology is improved upon by the implementation of automated optimization algorithms which mimic the manually iterative

process in an automatic fashion. The inverse analysis of data from thermal gravimetric analysis (TGA) and gram-scale experiments performed in the Controlled Atmosphere Pyrolysis Apparatus II (CAPA II) [13] is automated using hill-climbing algorithms and a custom fitness criteria. These optimization routines seek to maintain physically meaningful results by making iterations within highly constrained search space that is bounded by intuitive physical expressions, while improving accuracy and reducing labor intensity compared to manual inverse analysis. In addition, the fitness criteria similar to the coefficient of determination improves accuracy by quantifying the quality of a model prediction and thus removing visual bias inherent to manual analysis.

1.2 Previous Works

1.2.1 Model Parameterization

Since the development of numerical pyrolysis solvers (FDS, Gpyro, ThermaKin) about a decade ago, many researchers have undertaken the challenge of solving the complex inverse problem to parameterize material properties during pyrolysis. It should be noted early on that for any optimization scheme (automated or manual), questions of a solution's existence, uniqueness, and stability is inherent to the nature of inverse analysis of experimental data of any kind, and not solely an indicator of the capability of the optimization methodology [8]. For example, deficiencies in quality of measurements or experimental conditions may create a data set that has no real optimum solution or has a solution that is not actually representative of the true material performance. Likewise, all solutions found through inverse modeling should be considered as a linked parameter set; that is, the solution is a result of assumptions, boundary conditions, and formulations made by the numerical solver and may not be repeatable outside

of this framework [8]. Therefore, quality of measurement metrology should be regarded with equal importance to the quality of the analysis. A review of notable studies is presented here.

The most popular optimization methodology is the genetic algorithm [4]. Genetic algorithms are a type of evolutionary algorithm inspired by the theory of evolution proposed by Charles Darwin in "The Origin of Species by Means of Natural Selection" [14]. They are characterized by bio-inspired processes including mutation, crossover, and selection. Genetic algorithms have been applied extensively to optimizing properties of materials tested in TGA [15,16], cone calorimetry [11,17,18], and FPA [19,20] experiments. The popularity of this algorithm has been recently displace by applications of alternative algorithms which have been shown to provide greater efficiency, robustness, and accuracy [4,19].

A stochastic hill climber algorithm was first applied by Webster [18] and compared directly to GA in performance evaluated by ability to predict cone calorimetry MLR histories of a composite carpeting material and a fiberglass-reinforced polyester paneling material at multiple fluxes. The author extensively considered the range of validity of the solution sets to determine the physicality of results by both comparing individual properties to known measures and extrapolating the parameter sets against cone calorimetry tests at different fluxes. It was found that if parameters were left unbounded, the algorithms would produce highly unrealistic values. The SHC performed significantly better than the GA in terms of extrapolated results, despite some highly unrealistic material values. This study represented the highly composite materials as solely a mixture of homogenous virgin and char material. The heterogeneity of this fuel adds significant complexity to the already complex problem.

A follow-up study [11] worked another comparison of GA and SHC with a more homogenous fuel, polyvinyl chloride (PVC), evaluated with both cone calorimetry and flame spread models. It was found that outside of the calibrated domain, particularly for lower fluxes

where pyrolysis chemistry becomes more important, model predictive ability is limited. This study noted that the global one-step Arrhenius type reaction was not sufficient to capture the kinetics of decomposition, recommending preliminary TGA tests for better characterization.

Lautenberger and Fernandez-Pello [4] compared the performance of three popular algorithms (GA, SHC, SCE) with the addition of a hybrid genetic algorithm/simulated annealing (GASA) algorithm. Performance was evaluated by the algorithm's ability to reproduce each parameter of a synthetic dataset representing a three-component, two reaction scheme from manufactured temperature and mass loss rate data at two fluxes. The SCE algorithm was successful in all cases (finding all parameters within 1%), showing a clear advantage over the other algorithms and its ability to find the true global solution. However, the ability to find a global solution of an idealized curve from synthetic data does not guarantee similar convergence performance from real experimental data.

A major deficiency of using MLR measurements from cone calorimetry and FPA experiments as an inverse analysis target is the uncertainty introduced by solid oxidation effects prior to ignition and flame heat flux returning to the sample. Solid oxidation may or may not be a feature of full scale fires, because in many scenarios, a material is heated by an impinging flame and is not exposed to ambient oxygen prior to ignition. Attempts have been made to quantify flame heat feedback during cone calorimetry experiments, but the uneven distribution of heat feedback makes implementation into models a difficult task [21]. Therefore, studies using FPA or CAPA apparatus with nitrogenated atmospheres attempt to circumvent this issue by use of anaerobic gasification chambers with constant applied radiant flux.

Chaos et al. [19] compared the performance of a shuffled complex evolution (SCE) algorithm to a GA for parameter extraction from modified FPA experiments in nitrogen on poly(methy methacrylate) (PMMA), single-wall corrugated board, and chlorinated polyvinyl

chloride (CPVC). It was found that the SCE could determine material properties from MLR measurements with greater accuracy and considerably reduced iterations compared to the GA. This study made attempts to continuously measure sample surface temperature using an infrared pyrometer to give the algorithm another inverse analysis target and improve confidence in results. However, this data was never used because these measurements are highly dependent upon accurate surface emissivity characterization which is not always well defined during pyrolysis. Subsequent studies [20] made attempts of utilizing these temperature measurements while addressing this uncertainty, recognizing that any systematic error in these measurements would be manifested as an underestimation of temperature.

Over the course of many studies [12,22–27], Stoliarov et al. developed a manual methodology at the University of Maryland combining a hierarchy of milligram-scale and gram-scale experiments to manually undertake parameterization with as many direct measurements and few inferences as possible. The hierarchy of experiments attempts to isolate individual processes and variables in well-defined tests for either direct measurements of properties or inverse analysis with fewer compensation effects. While inverse analysis is still required for some property evaluation, the isolation established by the hierarchy of experiments ensures analysis is sufficiently well defined for a solution to be found with only a few manual iterations [25]. The hierarchy begins with TGA and DSC experiments such that the reaction kinetics and thermodynamics can be determined from isolated analysis based on a thermally thin assumption. Similarly, Microscale Combustion Calorimetry (MCC) experiments allow for careful determination of complete heats of combustion of all gaseous decomposition products identified from TGA experiments. Optical properties and heat and mass transport properties are then considered and determined from bench scale tests including infrared radiation absorption measurements and gasification tests. Previous studies have demonstrated the

successful application of this methodology to a wide range of materials, including cellulosic, non-charring, and charring materials [12]. Perhaps the most novel part of this methodology is that the mass loss rate from the bench scale gasification tests is never used as a target for parameterization, and therefore can be employed for model validation.

The reformed methodology began with the development of the Controlled Atmosphere Pyrolysis Apparatus (CAPA), a gasification device built within the framework of the cone calorimeter to provide simultaneous measurements of mass loss rate and back surface temperature of a coupon sized sample [28]. This apparatus featured an infrared camera to measure back surface temperature in an attempt to solve the problems associated with thermal contact and invasiveness of thermocouple measurements. Reliable surface temperature measurements allowed use of temperature evolution for direct analysis of thermal transport properties. Notable limitations of the CAPA include its inability to produce accurate data for highly thermally stable and highly intumescent solids [13]. In addition, the apparatus' nitrogen purge attempts to emulate anaerobic pyrolysis beneath a diffusion flame by reducing the effects of oxidation, but the apparatus was unable to create a fully anaerobic environment (at full nitrogen gas flow, measurements of 2.2 vol.% oxygen were measured at the sample surface) [28].

In an attempt to improve upon these deficiencies, the CAPA II [13] was developed with improved boundary condition control and additional tools to measure and account for charring and intumescence. The gasification chamber was now implemented with cylindrical geometry for circular samples (rather than a rectangular) to reduce dimensionality by axisymmetric symmetry, and featured water-cooled walls to maintain well defined boundary conditions. In addition, improvements in nitrogen supply offered the ability to create a fully anaerobic atmosphere to eliminate the effects of oxidation. This apparatus is detailed further in

Section 2.3.2 and comprehensively elsewhere [13]. Combining well defined boundary conditions with high fidelity temperature and mass evolution measurements provides the framework to solve a well-defined inverse problem. The back surface temperature of these tests are manually inversely analyzed for parameterization of the effective thermal transport properties of the decomposing sample in its various intermediate states. The mass loss rate histories from these tests properly emulate the anaerobic decomposition of polymers under steady heating conditions, and are therefore sufficient for validation of fully developed models.

This study adopts this manual methodology and attempts to reduce the labor intensity by the application of automated optimization algorithms within its already well defined framework. Because the inverse problems to be solved are already constrained tightly enough to be solved manually, a hill climbing algorithm was selected for its simplicity of implementation.

1.2.2 Sensitivity Analyses

Considering the variety and complexity of parameterization methodologies, and the fact that many effective properties are determined with high uncertainties, several researchers have conducted sensitivity analysis to determine which material properties were most important to characterize accurately. Understanding both the role and sensitivity of each parameter helps in reducing dimensionality of parameterization to distribute efforts and resources accordingly.

Early work by Stoliarov et al. [29] using the newly developed ThermaKin sought to determine which parameters affected a model's ability to predict average MLR, peak MLR, and time to mass loss of polymers in a cone calorimetry test. Sensitivity analysis was performed by adjusting one parameter at a time while holding the respective others at their nominal values.

Findings showed that the reaction kinetic pair (defined by the Arrhenius pre-exponential factor, A, and activation energy, E), heat of reaction, h_r, and residual char yield, θ, were of greatest importance, and absorption coefficient and reflectivity were of somewhat importance.

A sensitivity analysis by Linteris [30] studied the effect of property variations on MLR of simulated PMMA. Findings here indicated the most influential parameters were heat of reaction and specific heat capacity, citing that changes in activation energy did *not* have impactful effects. However, the author notes that this discrepancy likely arises from the fact that variations of E were only made to represent the bounds of previously measured activation energies of PMMA, which, is a rather well established property in literature. In addition, the value of A was not examined in conjunction with E. Also noted in this study was a compensation effect between thermal conductivity and in-depth absorption, and that the thermal thickness or thinness of a material had a large effect on MLR predictions, particularly for time to ignition.

In his dissertation, Bal [31] extensively studied uncertainty and necessary complexity of pyrolysis models, including a thorough sensitivity analysis. The author also studied time to ignition of PMMA and bounded his analysis by the ranges of parameters found in literature. He found that the variation in measurements of heat capacity, absorption coefficient, and kinetic pairs (A and E) was responsible for the large changes in time to ignition.

Recognizing the importance of the kinetic pair in pyrolysis modeling, a necessary complexity sensitivity analysis was performed by Marquis et al. [5] on polyisocyanurate (PIR) foam to determine the whether the highly complicated kinetic reaction scheme could be captured in a simpler scheme. He used an evolutionary algorithm to optimize PIR decomposition kinetics at different heating rates with different levels of sophistication, ranging in complexity from 1 to 7 reactions. Evidence showed that the decomposition required at least

3 reactions to reliably capture the MLR of TGA decomposition. However, this study was not extended to the limited reactions effect of DSC predictions or bench scale mass loss rate predictions.

Based on these results and in the high importance of accurately determining the reaction kinetic parameters, the optimization of A, E and θ was made a high priority in this study. Heat capacity and absorption coefficient are presently measured directly in this methodology, so confidence was had in the ability to accurately capture these measures.

1.3 Verification Material Selection

The materials used for verification of these automation schemes were chosen to represent a wide range of decomposition complexity. The simplest decomposition scheme, characterized by single-step decomposition and the absence of charring, serves as a preliminary case where solutions are already well documented for validation. A more complex decomposition scheme, characterized by multi-step decomposition with concurrent reactions and the presence of charring serves as a good case to verify the robustness of the optimization schemes. To illustrate the methodology, the thermal decomposition of two types of poly(methyl methacrylate) (PMMA) and two types of rigid polyisocyanurate (PIR) foam are considered.

PMMA is arguably the most studied solid material in fire research due to its nearly ideal thermal decomposition behavior characterized by the absence of charring or swelling and a simple decomposition into principally the monomer [32]. Hence, it has served as common surrogate fuel and as benchmark material to understand a wide array of fire phenomena, including burning rates [33–35], flame heat fluxes [21,35,36], and flame spread dynamics [34,37–41]. In addition, its simple and well documented thermal decomposition reaction scheme make it a choice material for pyrolysis modeling studies using solid phase numerical

solvers. The depolymerization (“unzipping’) has been extensively investigated on both the molecular [42–44] and engineering model levels [1,6,7,22].

In the present study, PMMA was chosen as a simple test material for initial phases of algorithm development. The simple, single decomposition reaction has a theoretically unique solution and avoids complexities associated with overlapping reactions which (in terms of optimization) may have several partial solutions (local minima) distracting from the global solution (global minimum). Two PMMA materials were used, distinguished by their manufacturing process: a black PMMA manufactured by solution casting and a transparent PMMA manufactured by extrusion. It has been documented that as a result of molecular weight differences inherent to the manufacturing process, these materials exhibit slight differences in decomposition behavior, particularly on the milligram-scale level [7,45]. Therefore, these simple and highly similar yet subtly different materials serve as good training data to validate the optimization algorithms’ ability to identify and resolve fine differences within otherwise similar global schemes.

Rigid polyisocyanurate foam is a closed-cell thermal insulation material commonly used in construction for wall, flooring, and roofing applications. It is similar in composition to polyurethane (PUR) foam, while a greater degree of crosslinking during polymerization results in a foam with superior thermal and mechanical stability [46]. Rising concerns about the flammability of PUR foam in building applications and the tightening of building regulations has led to the rising popularity of PIR foam. However, PIR foam has recently received renewed attention following the 2017 Grenfell Tower fire in London. PIR foam in the exterior façade was considered to be a contributing factor in that rapid growth of a fire that claimed 72 lives [47].

PIR materials have a complex thermal decomposition scheme, characterized by many kinetic reactions and the formation of char that maintains nearly all of the material's original thickness. These materials present a challenge in pyrolysis modeling due to the complications of concurrent reactions, their porous structure, and the influence of blowing agents and potential fire retardant additives. In this study, two PIR foams serve as the antithesis material to PMMA, providing training data with highly complicated kinetic and thermophysical mechanisms that require vastly increased dimensionality to capture in a comprehensive pyrolysis model.

1.4 Overview

In this study, the verification materials described in Section 1.3 are tested experimentally and then modeled for parameterization in a hierarchical fashion, i.e. properties obtained from a set of foundational experiments are used for interpretation and analysis of succeeding experiments to extract more properties. For continuity, a description of materials and experimental methods is followed directly by a qualitative presentation of corresponding experimental results, which are used as targets for inverse analysis in ensuing sections for quantification of material properties. Next, the numerical framework to model each experiment is characterized to facilitate the analysis and/or optimization of each experiment, each of which is described in length in the subsections within Chapter 5. Chapter 5 also includes discussion of the implementation and selection of algorithms, as well as a discussion on computational time and efficiency. The results of all optimization and analysis in the form of the fully developed model is provided and compared to experimental results for validation in Chapter 6. A compilation of all material properties can be found in Appendix I. Annotated ThermaKin input files are also provided in Appendix II.

Chapter 2: Experimental

2.1 Materials

2.1.1 Poly(methyl methacrylate) (PMMA)

Both the cast and extruded PMMA (trade name Acrylite) were purchased in the form of large sheets of thickness 5.8×10^{-3} m from Evonik Industries. Each have a measured room temperature density of 1210 kg m^{-3}. All prepared samples were placed in a desiccator cabinet for a minimum of 24 hours to remove residual moisture prior to testing. Milligram-scale samples were prepared by mechanically shaving the material into strands using a slowly rotating drill bit. The strands were subsequently ground in a pestle and mortar to make a powder-like consistency. Gram-scale samples were prepared as described in Section 2.3.

2.1.2 Rigid Polyisocyanurate (PIR) Foam

The foam materials considered in this study are two commercially available rigid thermal insulation foams, referred to henceforth as Foam X and Foam Y. Both foams have a measured room temperature bulk density of 32 kg m^{-3}. Bulk material was sourced as 2 inch thick panels, and the aluminum foil laminate was removed. Manufacturer notes indicate the use of hydrocarbon gasses as a blowing agent and the addition of a flame retardant. All prepared samples were placed in a desiccator cabinet for a minimum of 24 hours to remove residual moisture prior to testing. Milligram-scale samples were prepared using a cryogenic grinder to create a powdered material. It should be noted that during this preparation process, any gaseous blowing agent harnessed within the pores is released and thus not accounted for during STA tests. Gram-scale samples were prepared as described in Section 2.3.

2.2 Milligram-scale Experiments

2.2.1 Simultaneous Thermal Analysis

Simultaneous Thermal Analysis (STA) was conducted using a Netzsch 449 F3 Jupiter, shown in Figure 2.1. Simultaneous Thermogravimetric Analysis (TGA) and Differential Scanning Calorimetry (DSC) experiments provide a foundation for the determination of the kinetics and thermodynamics of decomposition of thermally thin samples. The apparatus exposes symmetrical crucibles (one sample containing and one empty) to a prescribed convective heating program while simultaneously measuring mass evolution using a high sensitivity micro-balance and heat flow using symmetrical crucible thermocouples. Sample mass and heat flow is recorded as a function of both temperature and time.

Prior to each sample test, both empty crucibles are used for a baseline correction test under identical heating conditions to measure and correct for differences in environment, buoyancy effects, and asymmetry of the furnace and sample crucibles. Powdered samples were packed into platinum crucibles with lids to maximize thermal contact and heat flow sensitivity. A small hole was present in the lid to allow for the escape of gaseous decomposition products. All experiments were conducted in nitrogen to emulate anaerobic pyrolysis conditions occurring within a diffusion flame. The STA was calibrated in accordance with the user manual using well-defined standard samples.

Powdered PMMA samples of 4-7 mg were tightly packed into the crucible for testing. Tests were performed at a nominal 10 K min^{-1} heating rate, chosen consistent to prior experiments [48]. Tests were repeated 7 times for each material and results were averaged.

Similarly, tightly packed powdered foam samples of 4-7 mg were tested. Ten repeat tests were performed for each foam material at a nominal 10 K min^{-1} heating rate, and results were averaged.

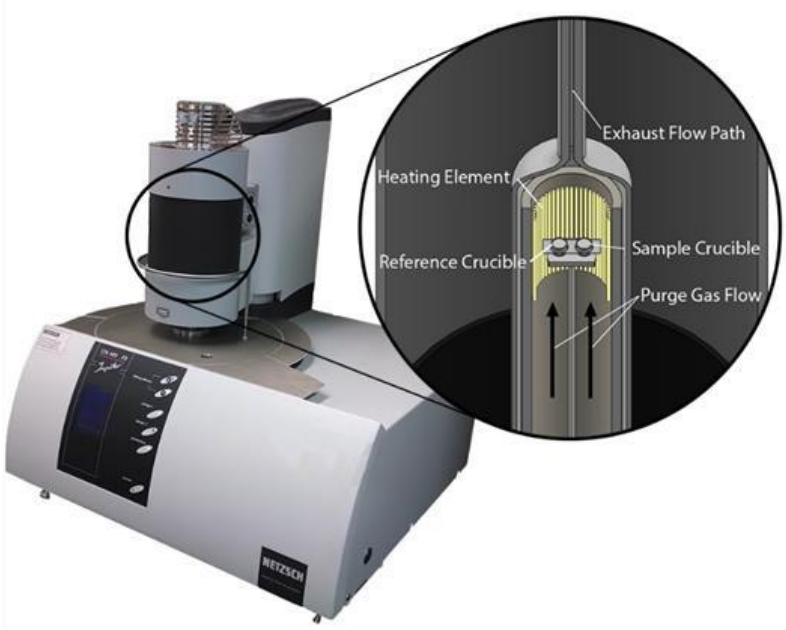

Figure 2.1: Simultaneous Thermal Analyzer

2.2.2 Microscale Combustion Calorimetry

The Microscale Combustion Calorimeter (MCC) [49] is an apparatus designed to measure the heat of combustion of gaseous pyrolyzates produced in an environment and configuration similar to that of the STA. Thermally thin milligram samples contained in an open-top ceramic crucible are exposed to a prescribed heating program in anaerobic conditions. Evolved gasses are transported from the pyrolyzer via flow of nitrogen to a combustor, wherein they undergo complete combustion in the presence of excess oxygen. The combustor was

maintained at a constant 1173 K, inducing a non-flaming oxidation reaction between the premixed gaseous pyrolyzate and oxygen supply. The nitrogen flow rate was set to 80 mL min^{-1} while the oxygen flow rate to the combustor was 20 mL min^{-1}. Using the principles of analytical pyrolysis, combustion gas analysis by oxygen consumption, and pyrolysis-combustion flow calorimetry (PCFC); heat release rate (HRR) data as a function of both temperature and time can be determined, as well as the heats of complete combustion of decomposition products from each reaction. A detailed description of the MCC can be found elsewhere [50], and a schematic of the apparatus setup is shown in Figure 2.2.

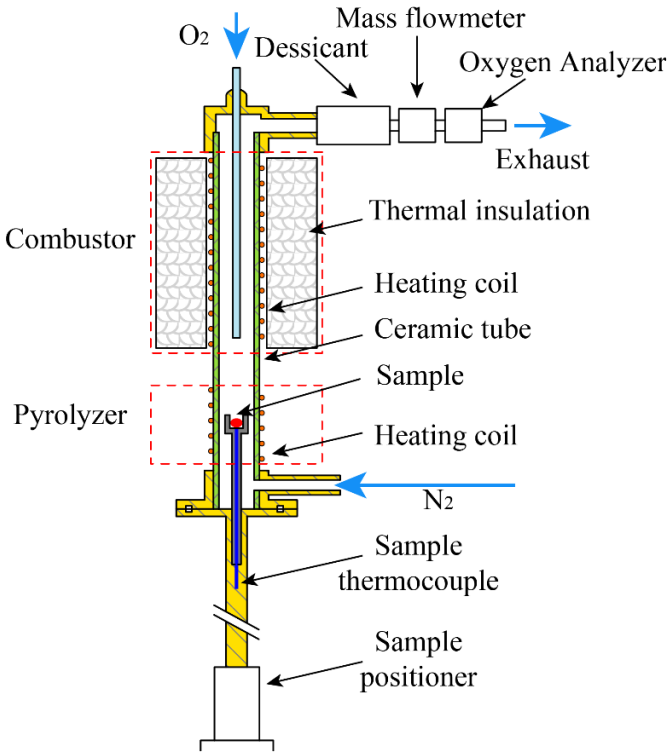

Figure 2.2: Schematic of Microscale Combustion Calorimetry

Samples used in this study were between 4 and 5 mg, and prepared similarly to STA samples. Powdered foam samples are tested under nominal 10 K min^{-1} heating (0.167 K s^{-1}) to maintain consistency with STA, and were repeated 5 times each. Powdered PMMA samples were tested at a faster 60 K min^{-1} (1 K s^{-1}) for 3 repeat tests, because this material has already been well studied on this apparatus and in literature. The tests showed a high degree of reproducibility. HRR data was recorded as a function of temperature and time. At the end of each test, the residual char yield was recorded and validated with TGA results.

2.3 Gram-scale Experiments

2.3.1 Broadband Radiation Absorption

Optical properties of materials necessary for further analysis were measured or approximated when not found in literature. Absorption coefficients were measured using a setup shown in Figure 2.3 following a methodology based on a technique by Linteris et al. [51] and later adopted in other studies [24,25,27]. The method entails irradiating a very thin (< 1 mm) sample with a conical heater and measuring transmitted radiation received by a Schmidt-Boelter type heat flux gauge with and without the sample in place. The radiation received by the gauge was collimated by a cylindrical hole within a Kaowool PM insulation board shield. The spacing from the bottom of the heater assembly to the sample was 9×10^{-2} m, at which flux was collimated flux reaching the gauge without the sample in place measured approximately 5 kW m^{-2}.

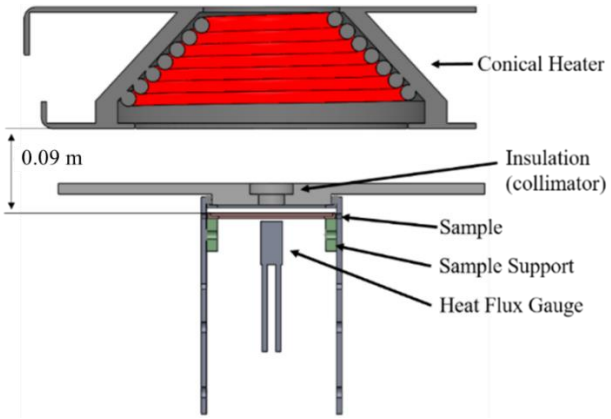

Figure 2.3: Schematic of apparatus to measure absorption coefficient

Incident radiant flux was measured for 30 s without the sample in place, followed immediately by a quick insertion of the sample and 3 seconds of data acquisition with sample in place. The acquisition was stopped to exclude contributions from conduction. Radiative heat through the sample was treated as one-dimensional parallel to the axis of collimation. The conical heater set point was chosen to represent an average flux between the high and low fluxes used during CAPA II experiments, which are described in Section 2.3.2, to produce a spectral range of radiant flux consistent with subsequent gasification experiments with the same heater. A generalized version of the Beer-Lambert law was used to derive absorption coefficient from these measurements [51], shown in Equations (1) and (2).

$$\kappa = \frac{2\ln(\varepsilon) - \ln(\tau_0)}{\delta} \tag{1}$$

$$\tau_0 = \frac{I_{x=\delta}}{I_{x=0}} \tag{2}$$

Where ε is the sample surface emissivity, δ represents the thickness of the exposed sample, measured to be 0.9×10^{-3} m, and τ_0 represents the ratio of radiant heat flux measured by the

heat flux gauge through the thickness of the sample ($I_{x=\delta}$) and with the sample removed ($I_{x=0}$). The machined PMMA samples used to measure absorption coefficient are shown in Figure 2.4.

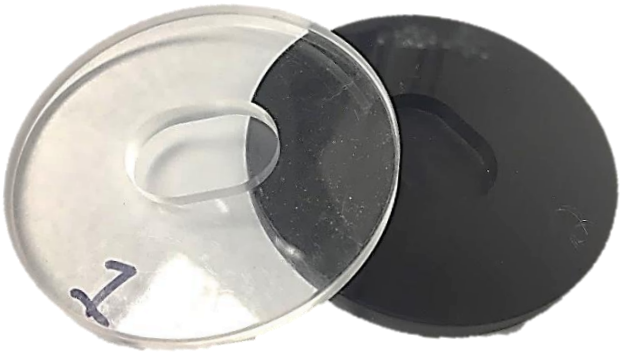

Figure 2.4: PMMA Samples prepared for absorption coefficient measurement. Collimated flux is directed through the thin (0.9×10^{-3} m) material in the center.

This methodology was not used for the foam samples, as it was deemed that machining the material down to a thickness of less than a millimeter would produce a structurally unstable sample with a heterogeneous surface and composition. Therefore, the foam samples were assumed to have a 'high' absorption coefficient (greater than 100 m^2 kg^{-1} or 3200 m^{-1}), consistent with findings of Günther et al. [46].

2.3.2 Controlled Atmosphere Pyrolysis Apparatus II (CAPA II)

The CAPA II, shown in Figure 2.5, is a gasification apparatus designed within the framework of the standard cone calorimeter to facilitate analysis of pyrolysis and thermal degradation of polymeric materials, including those exhibiting charring and intumescent behavior. This instrument provides well-defined boundary conditions and highly resolved simultaneous measurement of back surface temperature, mass, and profile (thickness) evolution for a sample exposed to radiant heat. The radiation, supplied from a conical electric

heater on a sliding rail for instantaneous application of heat, was carefully characterized to account for variation across the sample's surface, including the surface's angular orientation. The water cooled gasification chamber ensured consistent background temperatures, where convective heat losses from the front and back sample surfaces were further characterized through detailed simulations and validated against experimental measurements. Gasification chamber temperatures were monitored by thermocouples in several locations. Sample back surface temperatures were measured via a FLIR E40 thermal imaging camera for accurate, non-invasive, spatially resolved surface temperature measurements. Rates of gasification are measured by a Sartorius Cubis high resolution mass balance, sampling at 2 Hz. MLR evolution is post-processed using 5 s binning to smooth data and accumulate necessary statistics. Sample profile (thickness) evolution was monitored through a quartz observation window by a Logitech C930e camera mounted with the horizontal field of view coplanar with the top plane of the sample. These images are post processed to extract meaningful data representing the changes in material thickness. During the tests, a continuous purge of nitrogen at 185 L min^{-1} maintained the oxygen concentration in the gasification chamber below 1 vol. % to ensure that the measurements are free from oxidation effects, which simulates a solid burning under a continuous diffusion flame. Nitrogen flow was distributed around the circumference of the sample and introduced through a layer of glass beads (6.4×10^{-3} m diameter) to homogenize the flow and convective conditions on top. A detailed characterization of all CAPA II diagnostics and boundary conditions was carried out in an earlier study [13].

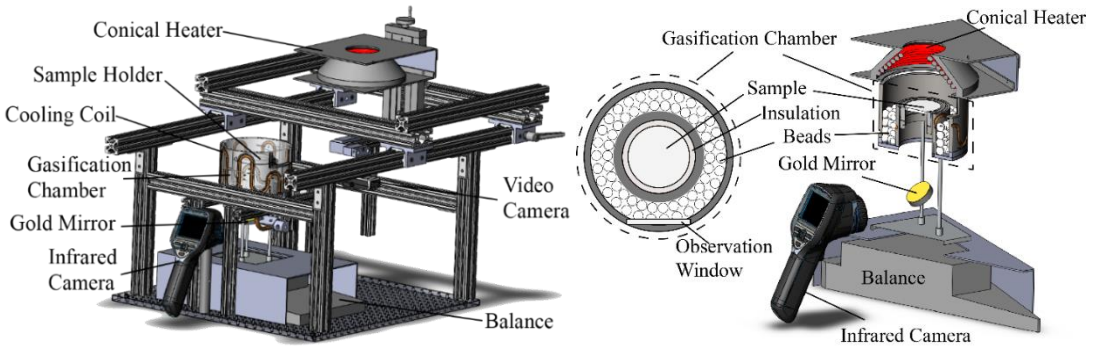

Figure 2.5: Schematic and cross-section of CAPA II apparatus

The current CAPA II tests were conducted at 25 kW m^{-2} and 60 kW m^{-2} of set radiant heat flux for PMMA, and 40 kW m^{-2} and 70 kW m^{-2} for the PIR foam samples. Higher flux was chosen for the insulation foams to compensate for the thicker material with lower conductivity. Samples were prepared using a hole saw to create 0.07 m diameter disks, with a thickness of 5.8×10^{-3} m for PMMA and 12.7×10^{-3} m for foam. Kaowool PM insulation was cut to tightly encircle the sample disks to create a nearly adiabatic radial boundary isolating heat transfer to the vertical dimension. Samples were then placed on thin copper foil to provide a homogeneous substrate with good thermal contact to measure back surface temperatures. The back side of the copper foil was painted with high temperature, high emissivity paint ($\varepsilon = 0.95$) allowing for reliable temperature measurements on the backside of the sample using the IR camera. Temperature measurements were made at 12 points representing 4 radial locations (r = 0, 0.01, 0.02 and 0.03 m from the center). Measurements were recorded until changes in mass loss and back surface temperature became insignificant. Experiments for each sample at each flux were performed twice to ensure reproducibility and accumulate statistics.

PMMA samples were adhered to the copper foil using high temperature epoxy to improve thermal contact and reduce the effects of swelling and warping. To account for mass

loss associated with thermal decomposition of the epoxy, independent TGA experiments were conducted on cured epoxy to determine the temperature of the onset of thermal decomposition and residual solid yield, found to be 589 K and 12%, respectively. Experimental CAPA II MLR histories were corrected by distributing the epoxy mass loss from the time at which the bottom temperature of the sample reached 589 K until the end of the test. These corrections were very minor; the total mass loss associated with the epoxy accounted for only about 1% of the measured PMMA mass loss.

During preliminary testing of PIR foam, it was found that the degraded residual material naturally adhered to the foil, indicating that good thermal contact was maintained throughout testing. Therefore, epoxy was not deemed necessary for these tests. A prepared foam sample including Kaowool insulation rings and copper foil substrate is shown in Figure 2.6.

Figure 2.6: PIR foam sample (Foam X) prepared for CAPA II experiments

Chapter 3: Experimental Results

A qualitative review of results of experimentation are as follows. The experimental data here is presented comparatively to demonstrate similarities and differences between respective materials (Cast vs. extruded PMMA, PIR Foam X vs. Y) before these data are used as targets for optimization and parameter quantification. The analysis and resultant quantification of all results is described and reported in Chapter 5. All uncertainties reported in this paper were calculated from the scatter of the experimental data and are reported as two standard deviations of the mean unless specified otherwise.

3.1 Milligram-scale Experiments

The results of PMMA milligram-scale experiments are shown in Figure 3.1. The decomposition of these materials is largely the result of a single decomposition reaction occurring around 600 K. The cast PMMA exhibits a reaction around 450 K that is most visible on the mass fraction curve of TGA experiments, that is hypothesized to be a reaction of the solvent used in the casting process. This reaction has an very minor contribution to MLR and heat flow. Both materials show a protuberance in the heat flow representative of the materials' glass transition, occurring at 378 K and 395 K for extruded and cast, respectively. Otherwise, the TGA and DSC profiles show a few notable differences between the two materials, most notably the peak MLR and peak heat flow of the main reaction, and the temperature at each major extremum. In addition, the onset temperature of the primary reaction is lower for the cast PMMA compared to the extruded counterpart. Similarly, differences in peak HRR as well as peak and onset temperatures from MCC are notable. Despite these HRR differences, a nearly perfect agreement is observed for the total heat release.

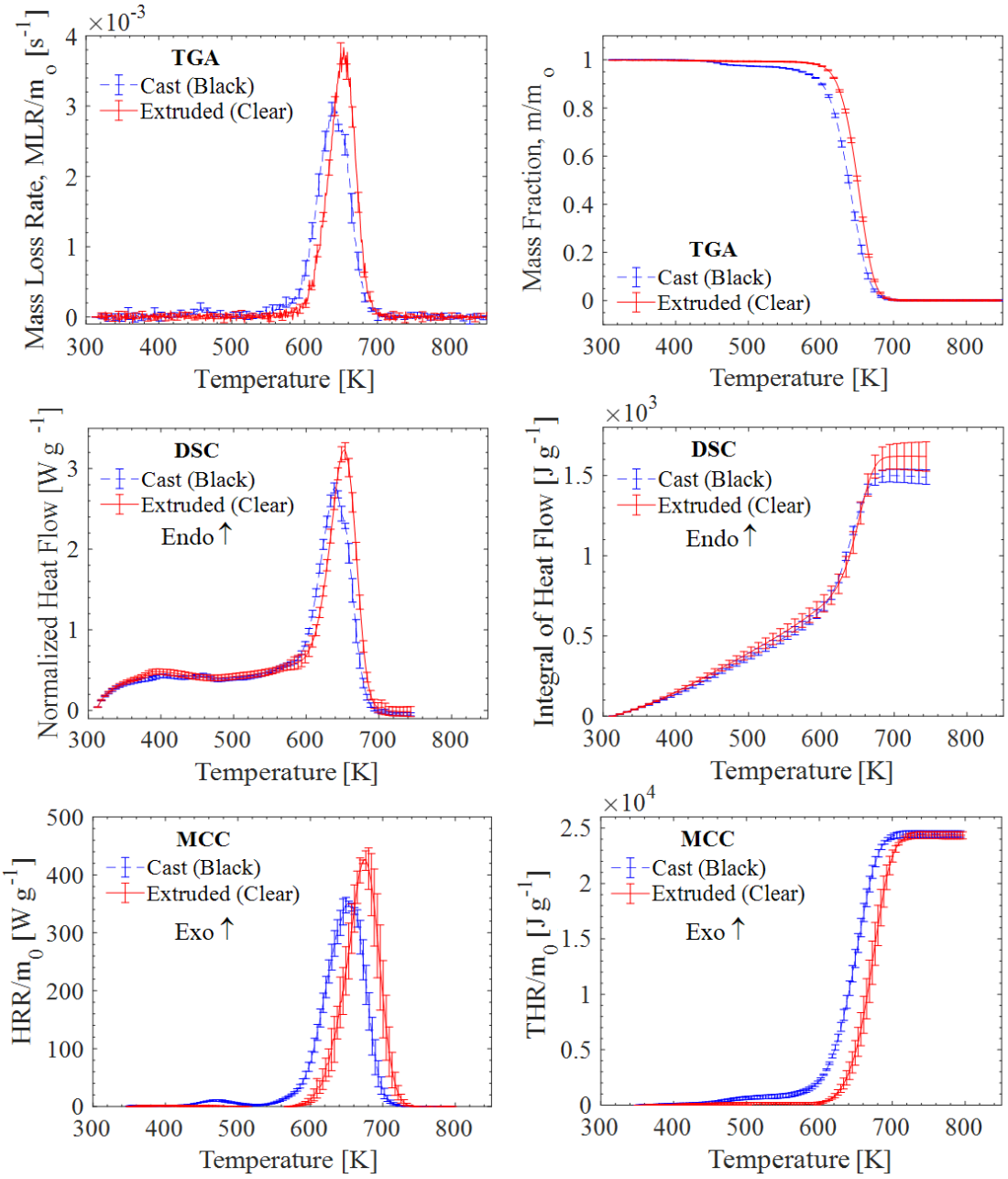

Figure 3.1: Averaged results of Milligram-scale experiments for extruded (red) and cast (blue) PMMA. TGA and DSC tests were performed at 10 K min^{-1} for 7 repeat tests, and MCC was performed at 60 10 K min^{-1} for 3 repeat tests.

The results of the PIR foam milligram-scale experiments are shown in Figure 3.2 and show much greater complexity than the PMMA samples. The two materials show strong similarity in the onset and offset temperatures of decomposition, but the intermediate reactions within show large differences. Similarly, the residual yield fractions, total heat flow, and total heat release are nearly identical. The exothermic reaction occurring for each foam around 600 K is characteristic of charring polymers, which, around this temperature begin to form char structures. These carbonaceous char structures are characterized by strong chemical bonds and release energy upon formation [23]. The most notable difference between the two materials is the peak MLR and the temperature at which this peak (and corresponding peak heat release rate) occurs: approximately 710 K and 600 K for foam X and Y, respectively. The MCC HRR data presented here and in Section 5.2.3 is normalized by initial sample mass.

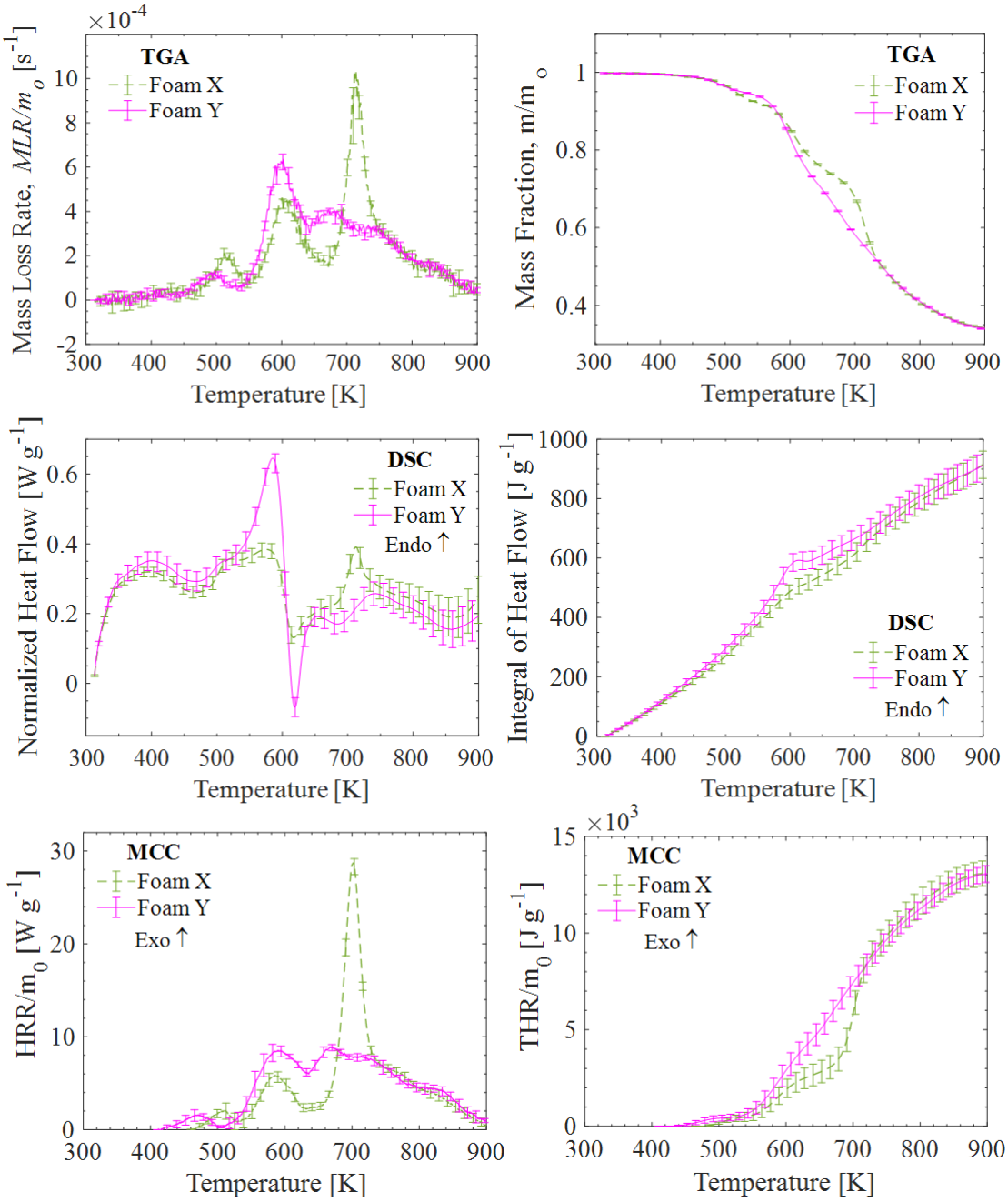

Figure 3.2: Averaged results of milligram-scale experiments for Foam X (green) and Y (magenta). TGA and DSC tests were performed at 10 K min^{-1} for 10 repeat tests, and MCC was performed at 10 K min^{-1} for 5 repeat tests. Data courtesy of Dushyant Chaudhari [52].

3.2 Gram-scale Experiments

Results of the gram-scale PMMA CAPA II gasification experiments are shown in Figure 3.3. The two PMMAs show great overall similarity in both back surface temperature (T_{back}) and mass loss rate (*MLR*) despite the differences noted in the milligram-scale results. Most notably, the time to mass loss for the cast PMMA is significantly shorter for both fluxes, primarily a result of the higher absorption coefficient (detailed in Section 5.3.2) and lower temperature onset of decomposition observed from the milligram-scale tests. Time to gasification is analogous to time to ignition, which is an essential measure to capture in fire modeling. The profile evolution from PMMA experiments is not presented here, as the material ablates evenly and steadily in a very predictable manor.

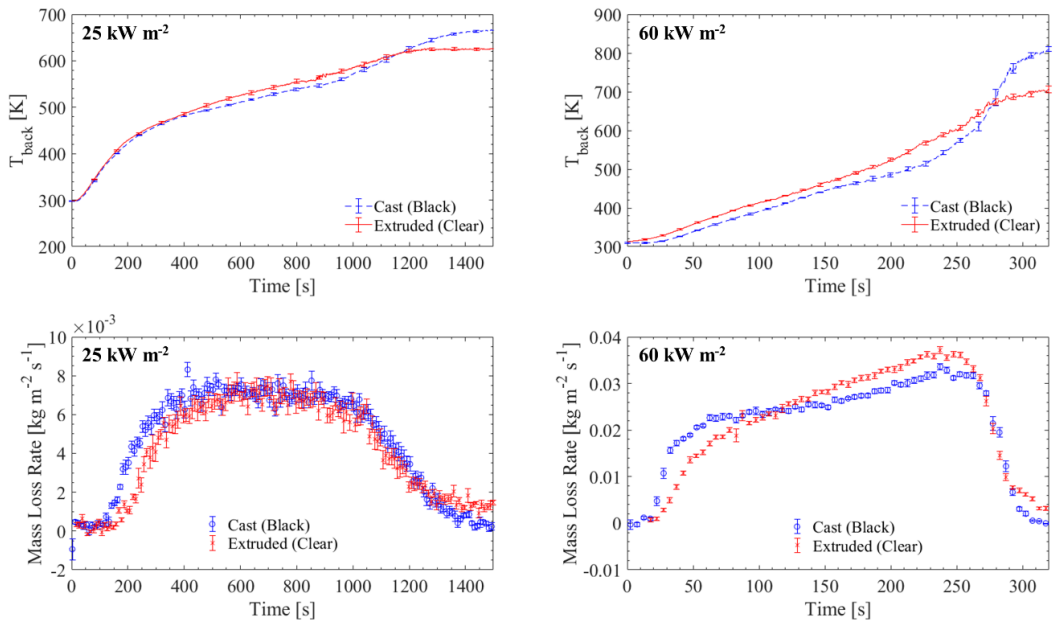

Figure 3.3: Experimental results of CAPA II tests for PMMA. Results are shown as the average of two tests, MLR data is smoothed by 5 s binning.

Results of the gram-scale foam CAPA II gasification experiments are shown in Figure 3.4, and exhibit strong similarities. In general, Foam Y shows better insulating properties in the sense that it maintains lower back surface temperatures for both fluxes. This temperature difference is not a pronounced for the 40 kW m^{-2} tests, where MLR and mass fraction histories show strong consistency. For the higher flux case, Foam Y experiences slightly less overall mass loss during the 15 minute duration of the experiment. This result comes as a slight surprise considering TGA tests show nearly identical residual yield mass fractions for the two materials. This dissimilarity is likely a result of the lower sample temperatures throughout the Foam Y tests. Also notable is the fact that the final mass fraction at the end of the 70 kW m^{-2} test falls below the final mass fraction of TGA tests. This result suggests there may be mass loss associated with the blowing agent gasses within the foam pores that are not accounted for in TGA tests due to the crushing in sample preparation. This is not evident for the lower flux, where by the time the test was terminated after 15 minutes of heating at 40 kW m^{-2}, it was found that the samples had not completely degraded for both materials, as evident by the sample cross section showing a gradient ranging from original sample color to char, shown in Figure 3.5. This indicates the residual yield should not be expected to be consistent with the TGA char mass fraction, and may mean the blowing agent within the samples is not completely released during testing. The blowing agents within the samples may be different in for each material, which may also contribute to the discrepancy of mass fractions at the high flux. Similarly, only the profile evolution from the 70 kW m^{-2} experiments is presented here, as the partially-degraded 40 kW m^{-2} do not produce a full picture of the materials' expansion/contraction behavior. Foam X experiences only contraction during the duration of testing, while Foam Y experiences slight swelling during the first several seconds (~40 s) of heating followed by gradual contraction.

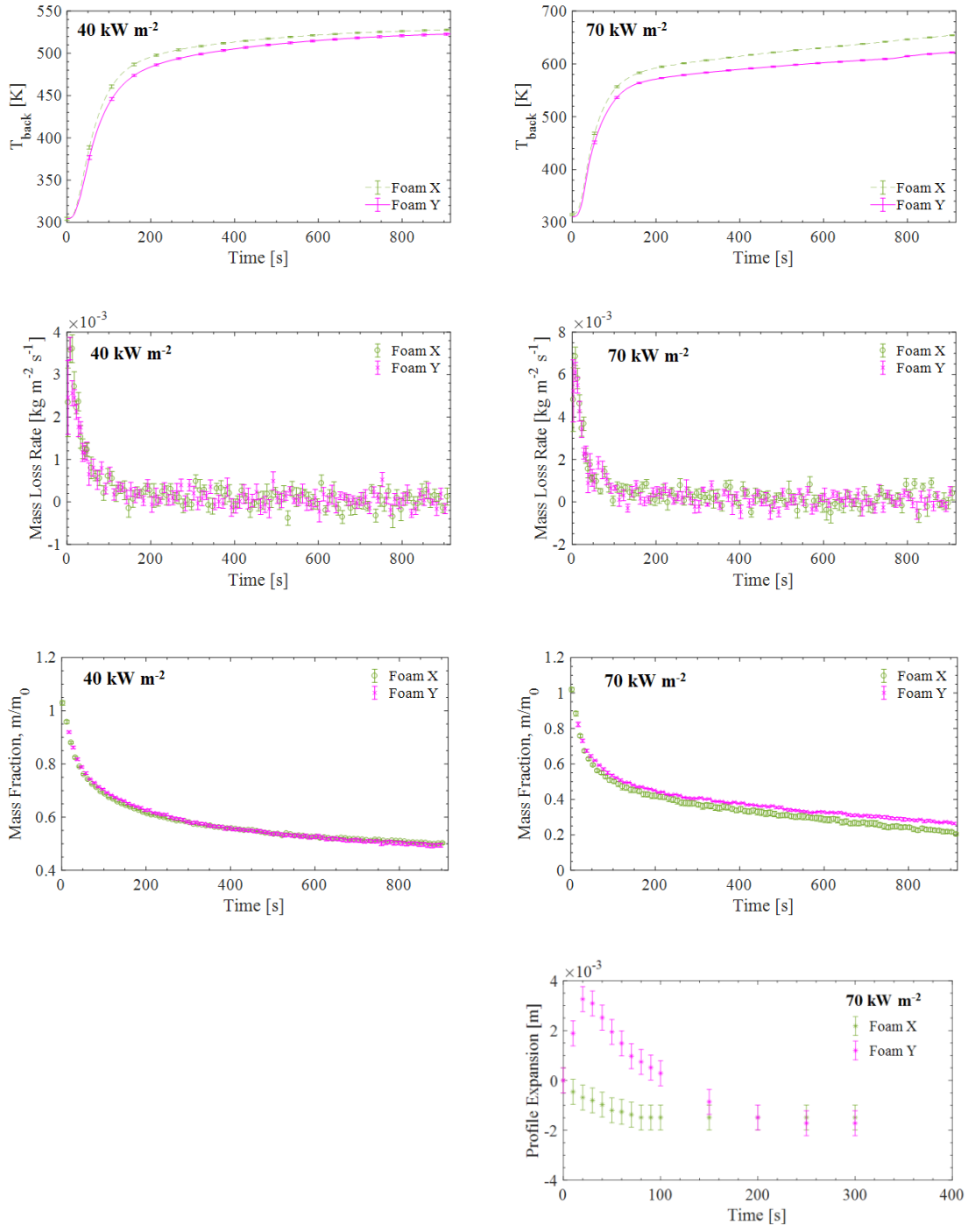

Figure 3.4: Experimental results of CAPA II tests for PIR Foam. Results are shown as the average of two tests, MLR data is smoothed by 5 s binning.

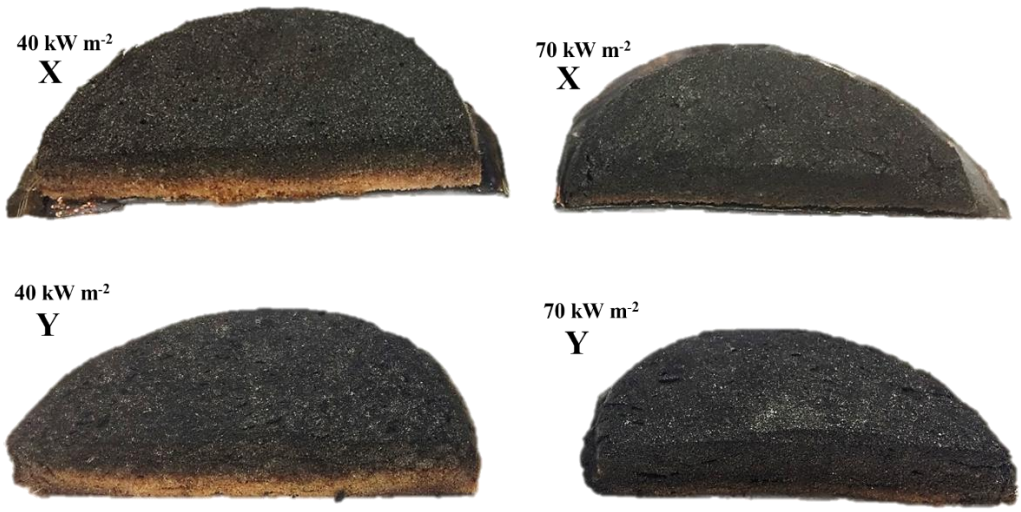

Figure 3.5: Exemplary PIR foam sample char structures at termination of CAPA II tests, low and high flux

The two groups of materials, PMMAs and foams, exhibit vastly different thermal decomposition behavior, and the specific varieties of each materials show subtle yet important differences that should be captured in a pyrolysis model. Hence, it was determined that this dataset provides good criteria to test the ability of optimization algorithms to identify and resolve this range of differences in the development of comprehensive pyrolysis models. The development methodology is summarized as follows.

Chapter 4: Numerical Framework – ThermaKin

Modeling was handled using ThermaKin 2Ds, a comprehensive numerical pyrolysis solver developed to predict the behavior of various materials in response to external heating. Recent developments have introduced the framework for one- and two- dimensional simulations in Cartesian and cylindrical coordinates. ThermaKin computes the transient rate of gaseous fuel production by solving non-steady energy and mass conservation equations formulated in terms of finite elements. A comprehensive description of governing equations, numerical implementation, and validation can be found in prior publications [2,53].

ThermaKin interprets decomposition schemes as a progression of user-defined reactions describing the evolution of a material's mixture of *components* in an environment defined by parameters called *conditions.* Components are modules that describe solid and gas phase material that describe the mass considered in the system, each of which is parameterized by a full set of properties including density, heat capacity, thermal conductivity, gas transfer coefficient, emissivity, and radiation absorption coefficient. Typical polymer decomposition schemes involve a virgin material component, several intermediate components representing various states accounting for physical and chemical transitions during heating, and eventually a char component. Conditions describe simulation dimensionality and coordinates; object structure and geometry; boundary, heating, and mass transport conditions; and integration parameters (resolution). Specific components and conditions used in this study are as follows.

4.1 Components

Global reaction schemes were determined by qualitatively inspecting STA data to identify the minimum number of reactions required to capture the kinetics and thermodynamics of decomposition.

4.1.1 PMMA Components

For the PMMAs, the global reaction mechanism was defined as a single first-order decomposition reaction for extruded PMMA, and two first order reactions in series were designed for cast PMMA. A glass transition was defined for both materials to accommodate for the protuberance in the heat flow curve observed just below 400 K, described in Section 3.1. The glass transition was implemented into the model as a reaction with no associated kinetics or heats of decomposition. This implementation allows material properties, namely specific heat capacity and thermal conductivity, to be changed at a defined temperature to account for observed discontinuities. The global reaction scheme as implemented into ThermaKin with place-holding stoichiometric coefficients, θ, is shown in Table 4.1.

Table 4.1: Global reaction scheme for PMMA

Extruded (Clear) PMMA		Cast (Black) PMMA	
#	**Reaction**	**#**	**Reaction**
1	$PMMA \rightarrow PMMA_{melt}$	1	$PMMA \rightarrow PMMA_{melt}$
2	$PMMA_{melt} \rightarrow \theta_2\, PMMA_{char} + (1\text{-}\theta_1)MMA_{gas}$	2	$PMMA_{melt} \rightarrow \theta_2\, PMMA_{int} + (1\text{-}\theta_2)MMA_{gas}$
		3	$PMMA_{int} \rightarrow \theta_3\, PMMA_{char} + (1\text{-}\theta_3)MMA_{gas}$

4.1.2 PIR Foam Components

For the foam samples, many more reactions were required to capture the complexities observed in the STA data. For Foam X, five consecutive first-order reactions and one second-order reaction was identified. Each reaction resulted in an individually defined gaseous component so that each evolved gas could be assigned a unique heat of combustion. The decomposition of Foam Y was represented by seven consecutive first-order reactions. The global reaction scheme as implemented into ThermaKin with place-holding stoichiometric coefficients, θ, is shown in Table 4.2.

Table 4.2: Global reaction scheme for PIR foams

Foam X		Foam Y	
#	**Reaction**	**#**	**Reaction**
1	$FoamX \rightarrow (1-\theta_1)GAS_1 + \theta_1 INT_1$	1	$FoamY \rightarrow (1-\theta_1)GAS_1 + \theta_1 INT_1$
2	$INT_1 \rightarrow (1-\theta_2)GAS_2 + \theta_2 INT_2$	2	$INT_1 \rightarrow (1-\theta_2)GAS_2 + \theta_2 INT_2$
3	$INT_2 \rightarrow (1-\theta_3)GAS_3 + \theta_3 INT_3$	3	$INT_2 \rightarrow (1-\theta_3)GAS_3 + \theta_3 INT_3$
4	$INT_3 \rightarrow (1-\theta_4)GAS_4 + \theta_4 INT_4$	4	$INT_3 \rightarrow (1-\theta_4)GAS_4 + \theta_4 INT_4$
5	$INT_4 \rightarrow (1-\theta_5)GAS_5 + \theta_5 INT_5$	5	$INT_4 \rightarrow (1-\theta_5)GAS_5 + \theta_5 INT_5$
6*	$INT_5 + INT_5 \rightarrow (2-\theta_6)GAS_6 + \theta_6 CHAR$	6	$INT_5 \rightarrow (1-\theta_6)GAS_6 + \theta_6 INT_6$
		7	$INT_6 \rightarrow (1-\theta_7)GAS_7 + \theta_7 CHAR$

**Foam X Rxn #6 is a second-order reaction*

Supplementary TGA experiments were performed with oxygen introduced in atmospheric proportions to oxidize the charring polymer. The residual yield from these experiments consisted of a fibrous material assumed to be similar in composition to the glass fiber considered in a previous study of glass fiber reinforced polyamide 66 by Ding et al. [27]. A glass fiber component was introduced as an inert component that was not involved in any defined reaction. The properties of glass fiber were taken from the study by Ding et al. [27]. The proportion (mass fraction) of glass fiber in the virgin material mixture was defined based on mass fraction yields from the oxygenated TGA tests, 0.052 and 0.041 for foam X and Y, respectively.

4.2 Conditions

All simulations presented in this study were performed with a temporal resolution of 0.01 s. Every integration parameter was varied by a factor of two until convergence was demonstrated by comparing simulation results. Parameterization for emulation of experimental conditions are as follows.

4.2.1 Milligram-scale Simulations

Milligram-scale tests are simulated using a single spatial element, representing the thermally thin sample used for TGA, DSC, and MCC tests. Heating conditions were defined as a convective source with very high convective coefficient (1×10^5 W m^{-2} K^{-1}) at the boundary so that the temperature of the element followed the experiment. Gaseous mass transport conditions were defined such that gaseous products experienced no resistance to outflow. The experimental heating rate, dT/dt, was parameterized by a decaying sinusoid as a function of experimental time, t, to account for variation in instantaneous heating rate, particularly during the beginning of the tests. The nominal 10 K·min^{-1} heating rate averaged from the 14 PMMA STA tests produced the heating rate shown in Figure 4.1 and can be parameterized by Equation (3).

$$\frac{dT}{dt} = a\{1 - exp(-bt) \times [cos(ft) + g\, sin(ft)]\} \tag{3}$$

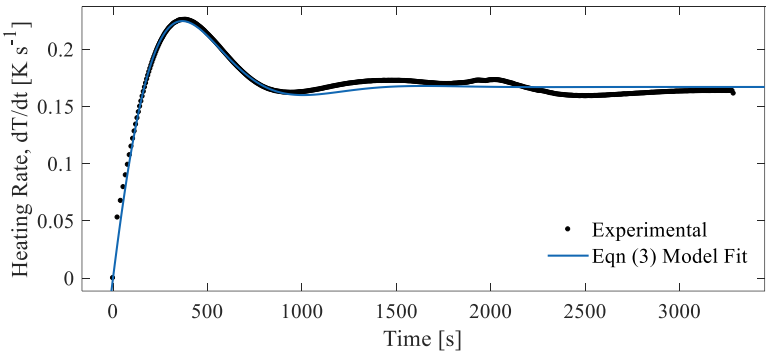

Figure 4.1: Experimental heating rate, fitted by decaying sinusoid for STA simulations

The fit in Figure 4.1 and Equation (3) used the following parameters: a = 0.167 K s^{-1}, b = 0.0034 s^{-1}, f = 0.0049 s^{-1}, and g = -1.02.

Likewise, a similar procedure was followed to characterize the experimental MCC heating rate of nominal 60 K min^{-1} (1 K s^{-1}) from the foam MCC experiments. The MCC boundary conditions were prescribed to ThermaKin similarly to the STA simulations, with a high convective coefficient (1×10^5 W m^{-2} K^{-1}) at the boundary and no influence of flame or external radiation. The spatial resolution and integration parameters were identical to STA simulations, maintaining the thermally thin assumption.

The PMMA MCC experiments were not modeled for analysis because decomposition results in only one decomposition product. Therefore, this sole product can be characterized directly by integration of experimental data without inverse modeling. This is described fully in Section 5.2.3.

4.2.2 Gram-scale Simulations

The 2D axisymmetric mode of ThermaKin was developed with the goal of building a framework to accommodate for charring and intumescent materials in a cylindrical geometry simulating that of the CAPA II. This mode allows for more detailed descriptions of boundary conditions that are spatially resolved, and can account for heat and mass transfer processes within the sample in the radial direction. Likewise, the ability to numerically capture expansion and contraction allows for significantly more accurate predictions of rates of gasification for challenging intumescent materials such as poly(vinyl chloride) (PVC) and Bisphenol A poly(carbonate) (PC) [54]. In the present study, CAPA II PMMA experiments showed steady ablating that was uniform across the sample radius. CAPA II PIR foam experiments experienced slight swelling and contracting, particularly during initial moments of heating, but thickness across the sample radius remained mostly uniform for the entire duration. Therefore, to reduce dimensionality and improve computational times of simulations, radial variations

were not considered for the CAPA II simulations of all materials. Simulations were implemented using a single radial element of 0.035 m and $\delta = 5\times10^{-5}$ m spatial discretization, thus creating a 1D simulation. These 1D simulations within the framework of the 2D axisymmetric mode enables both fast computational times and highly characterized boundary conditions from CAPA II. More specifically, the 2D axisymmetric mode allows for description of spatial and radial variation of radiant heat to emulate the measured variation of the conical heater of the CAPA II and more descriptive heat loss conditions on the boundaries.

The radiative and convective boundary conditions on the top boundary were characterized from experimental measurements and CFD simulations. Previously, Swann [13,54] measured the temperature histories and convection coefficient of the nitrogen purge flow on the top boundary as a function of external heat flux and radial position, and accordingly characterized losses specific to each flux. Similarly, the radiant heat flux supplied by the conical heater was experimentally characterized, accounting for variations dependent upon radial, axial, and angular orientation. A full description of this characterization can be found in Swann's Ph. D. dissertation [54].

Since the variation of back boundary conditions is more sample dependent, the losses to the back boundary were specifically characterized according to measurements of background conditions during each material's CAPA II experiments. It was experimentally determined that background conditions for both PMMA were consistent enough to be characterized together. Conversely, the foam samples had enough background variation between materials (mostly due to the apparatus heating from consecutive testing) to be characterized separately. The evolution of experimental boundary temperatures for each material was characterized using piecewise functions to be implemented into the model, summarized in Table 4.3. ThermaKin uses these back boundary temperature profiles to calculate the convective and radiant contributions of the

background on the sample for the duration of the simulation. The back boundary convection coefficient was prescribed as 4 W m^{-2} K^{-1}, determined from prior CFD simulations of CAPA II [13,54].

Table 4.3: Back boundary conditions characterization for PMMA (combined cast and extruded) and each PIR foam material for each experimental flux.

Material	CAPA II Setpoint (kW m^{-2})	Back Boundary Temperature (K)
PMMA	25	$295 + 0.0163t$, $t \leq 800$ s 308 , $t > 800$ s
	60	$303 + 0.59t$
Foam X	40	$295 + 0.04t$, $t \leq 500$ s 315 , $t > 500$ s
	70	$305 + 0.0733t$, $t \leq 450$ s 338 , $t > 450$ s
Foam Y	40	$295 + 0.04t$, $t \leq 500$ s 315 , $t > 500$ s
	70	$295 + 0.0889t$, $t \leq 450$ s 335 , $t > 450$ s

Gaseous mass transport conditions were defined specific to each component, details of which are found in Section 5.3.1. Mass flow was not permitted through the bottom boundary, which was defined as a $\delta = 5\times10^{-5}$ m single-element of copper representing the copper foil used in experiments. The copper was not involved in any defined reaction but was simulated explicitly as a substrate to analyze back surface temperatures. The properties of copper were gathered from literature [55].

Chapter 5: Optimization, Analysis, and Model Parameterization

5.1 Overall Approach

A complete pyrolysis model requires parameterization of kinetics and thermodynamics of decomposition, heats of combustion of gaseous products, and thermal transport properties of condensed-phase components during thermal degradation. This work adopted a hierarchical approach wherein simpler, more fundamental tests were modeled and analyzed before proceeding to higher complexity. The result is a methodology in which properties can be determined from well-defined conditions. An emphasis was placed on taking simple, systematic steps in this analysis to create a model with appropriate complexity in a reproducible methodology. Specifically, the order of analysis was: TGA, DSC, MCC, followed by the absorption coefficient and CAPA II experiments. A review of all material properties presented in this chapter will be compiled in Appendix I. Details of each analysis are described as follows.

5.1.1 Optimization Framework

Optimization algorithms were implemented by looping instances of the ThermaKin application as a subroutine within MATLAB. Overhead within the MATLAB implementation between loops was light; the efficiency of optimization time was dominated by the CPU time of each ThermaKin simulation. Parallel processing is not currently implemented, but is discussed in Section 7.4. Hill climbing algorithms were chosen primarily for their simplicity.

Hill climbing is a heuristic search algorithm designed for optimization of problems with a large number of optimizable elements. These algorithms attempt to maximize a function by iterating individual elements within a vector. In this context, the algorithm is designed to maximize a custom fitness function (quantifying the similarity of simulated curves with

experimental data curves) by iterating and optimizing the vector of material parameters that are inputted into the model simulation. Each step involves a change to only one parameter and an evaluation of fitness, accepting the step if improvement is made over the current guess. Optimization is run until successive guesses yield no improvement over the current guess. This implementation has the benefit of being an anytime algorithm; that is, the current best solution is returned even if the program is interrupted before completion. In many cases, a satisfactory result was found before the total prescribed duration, and the user would choose to break the loop early.

The optimization algorithms in this study are further classified as steepest ascent hill climbing algorithms. The distinction of this variation from a typical hill climbing algorithm lies in the number of successive guesses that are compared before a step is chosen. In this case, nearly a dozen unique guesses of different step sizes of a single parameter are made, and only the best guess is chosen as the next step. While increasing computational time over traditional hill climbing, this implementation allows the program to elect variable step sizes and provides some resistance to converging on local maxima instead of global maxima.

A discussion of computational efficiency and run times for each optimization program is discussed at the end of this chapter, under Section 5.4.

5.2 Milligram-scale Analysis

Latter steps of the hierarchical development process are dependent upon accurate parameterization of properties extracted from foundational milligram-scale tests. Therefore, much emphasis was placed on the accuracy, uniqueness, and meaningfulness of properties obtained from these tests. Of the properties extracted from milligram-scale tests, the reaction kinetics, A, E, and θ, are simultaneously the most difficult and important properties to

parameterize [29]. The compensation effects between A and E make this parameterization additionally difficult and labor intensive, and decomposition schemes with a multitude of reactions can vastly increase dimensionality of this problem. Therefore, an optimization program was developed to automate this difficult task. Once the reaction kinetics are determined, it is a relatively straightforward task to parameterize the heats of reactions and heats of combustion, as these require only a single property to fit per component. Therefore, these analyses were optimized manually and did not require automation. The details of each analysis is described as follows.

5.2.1 Optimization: Arrhenius Parameters

The Arrhenius parameters, namely the pre-exponential factor, A, and activation energy, E, are the defining parameters of decomposition for Arrhenius-type reactions in a thermally thin scheme. In addition, the solid phase residual yield, θ, is essential to the description of decomposition. These parameters are determined by inverse analysis of data averaged from TGA experiments conducted in accordance with Section 2.2.1. The conditions and components used in ThermaKin simulations have been described previously in Section 4.2.1.

In the simplest, ideal reaction scheme, decomposition can be accurately captured using a single first-order global reaction, defined by a single triplet of A, E, and θ. Extruded PMMA is an example of such an idealistic case. In the more common case, a single decomposition reaction does not fully capture the complex kinetics of thermal decomposition. As such, it is sometimes necessary to define multiple consecutive and/or parallel reactions to fully capture the decomposition. A unique triplet of A, E, and θ must be determined for each defined reaction. For materials with increasing decomposition complexity, such as Foam Y, decomposition was best represented as a series of 7 consecutive first-order reactions, resulting

in 21 parameters to optimize. The optimization program presented in this section developed to be accommodating to a wide variety of materials with customizable levels of complexity.

Initial guesses for A and E are assigned to each reaction using an approximate solution to the first order Arrhenius kinetics under linear heating conditions, given by Lyon et al. [56], shown in Equations (4) and (5).

$$E = \frac{eRT_{peak}^2 MLR_{peak}}{m_o(1-\theta)\frac{dT}{dt}} \tag{4}$$

$$A = \frac{eMLR_{peak}}{m_o(1-\theta)} \exp\left(\frac{E}{RT_{peak}}\right) \tag{5}$$

In this set of equations, MLR_{peak} and T_{peak} represent the peak MLR and corresponding temperature associated with each reaction peak in the TGA MLR profile (normalized by initial mass, m_o). The value of MLR_{peak} and T_{peak} is determined by user input into a graphical user interface (GUI) which directs the user to locate each reaction peak, as shown in Figure 5.1. The condensed phase residual yields, θ, of each reaction is approximated programmatically based on reaction locations designated by user GUI (Graphical User Interface) input (see Figure 5.1), or can be manually inputted by user intuition based on intuition or visual inspection of MLR and Mass Fraction data from TGA. R is the universal gas constant, and dT/dt is the nominal TGA linear heating rate.

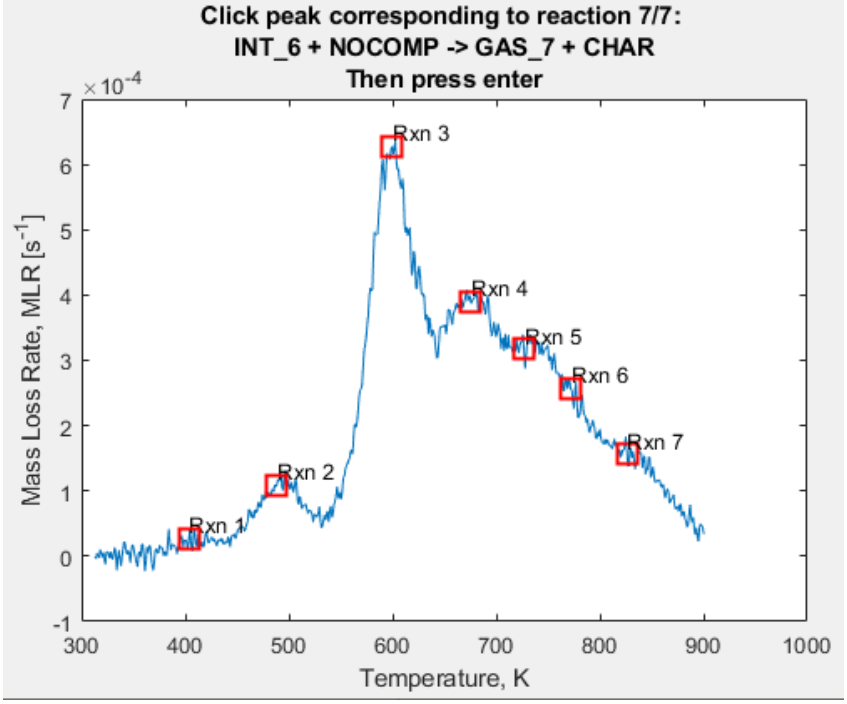

Figure 5.1: GUI for designation of Foam Y reaction peak locations.

In typical TGA optimization algorithms, iterative guesses of A and E would be made until a certain convergence criteria is met, based on some fitness criteria. In manual inverse analysis, iterations to MLR_{peak} and T_{peak} would be made, and A and E would then be subsequently recalculated until a certain convergence criteria is met, usually based on fitting the MLR peaks and onsets within their experimental uncertainty. In this case, the manual methodology is performed in an automated fashion, making iterative guesses of MLR_{peak} and T_{peak} in small, successive steps and programmatically recalculating A and E each iteration according to Equations (4) and (5). It was found that automating iterations directly to A and E provided less intuitive outcomes since there are compensation effects between the two [31,57]. The benefit of iterating MLR_{peak} and T_{peak} rather than A and E is exemplified in Figure 5.2. In Figure 5.2(a), iterations of MLR_{peak} and T_{peak} manifest their changes to reaction MLR in intuitive

vertical and horizontal increments in MLR vs. temperature space, respectively. Conversely, in Figure 5.2(b), where similar iterations are made directly to A and E, the compensation effect is highly evident and deteriorates the quality of guesses. This iterative process also maintains the benefit of retaining physical meaning in the search space as Equations (4) and (5) are derived based upon physically derived expressions [58].

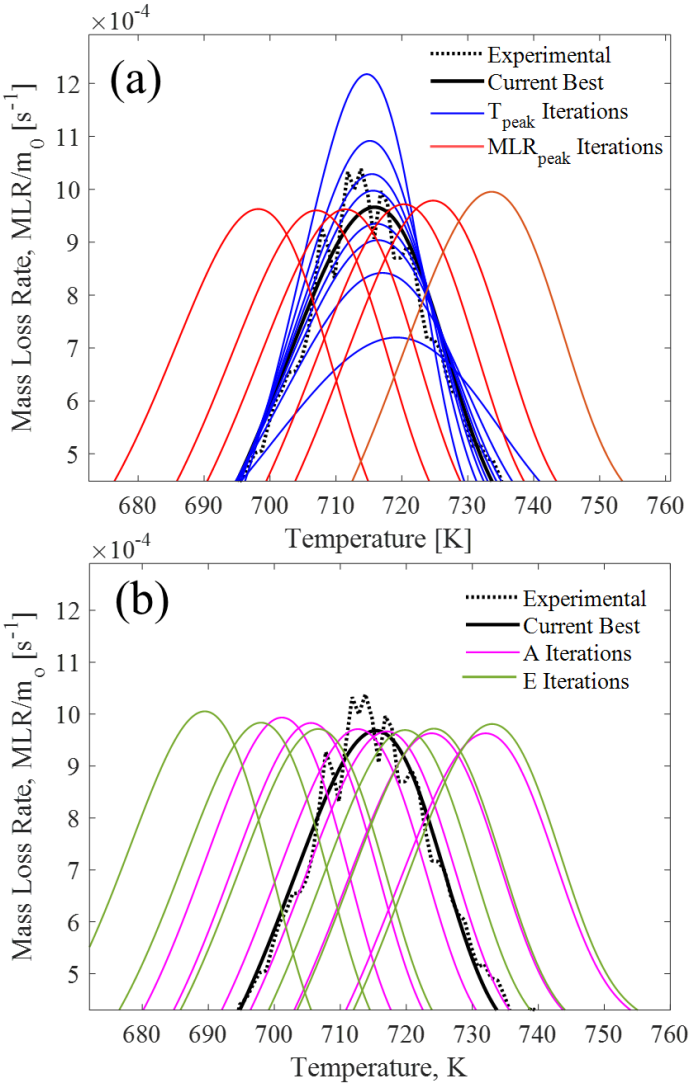

Figure 5.2: Search space produced by 6 iterations each of (a) T_{peak} and MLR_{peak} and (b) A and E. Compared to iterations of A and E, which compensate for each other, these manifest themselves almost perfectly in X vs. Y (MLR vs. Temperature) space.

The optimization target function is a modified coefficient of determination measuring the goodness of fit (*GoF*) of the model simulation with experimental data:

$$GoF = 1 - \frac{1}{Exp_{max}} \sqrt{\frac{\sum_{i=1}^{N} (Exp_i - Model_i)^2}{N}} \tag{6}$$

Here, at every experimental data point, the squared difference in experimental value (*Exp*) and model value (*Model*) is summed and normalized by number of experimental data points (*N*) and the maximum experimental value. This comparative metric is considered both in terms of MLR and mass fraction curves. In most cases, the MLR should serve as the dominant target of fitting, but the program features adjustable weighting of MLR and Mass Fraction fits. This weighting is calculated as:

$$GoF_M = \alpha (GoF)_{MLR} + (1 - \alpha)(GoF)_{Mass\ Fraction} \tag{7}$$

Where α is a scalar (0 - 1) representing the weight of MLR and Mass Fraction contributions, respectively. By default, α = 0.7, resulting in a 70/30 split of fitting weight in favor of MLR. This split weight was found to better target residual yields and thus assists in the optimization of θ over a purely MLR based fit. This quantification of fitness produces values such that a GoF_M of 1 indicates a perfect fit.

For each consecutive reaction in the pre-defined decomposition scheme, the program executes the following hill climbing algorithm, outlined in the logic diagram shown in Figure 5.3.

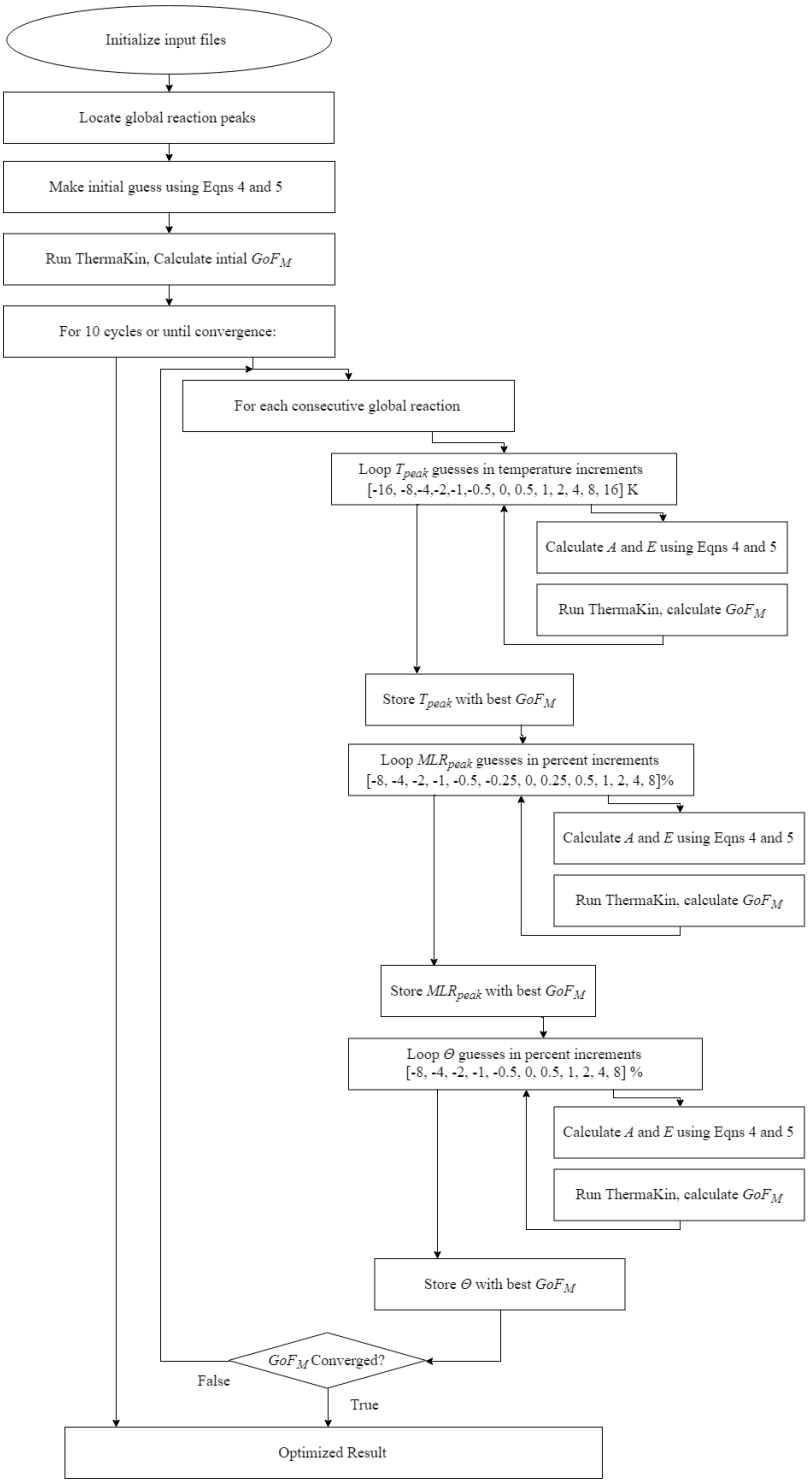

Figure 5.3: Logic diagram of program's algorithm for *A*, *E*, and θ optimization.

Note that each guess of T_{peak}, MLR_{peak}, or θ generates a unique pair of A and E by calculation. Despite stepping in only 1 parameter space, two parameters are adjusted. If values of θ for each reaction are known, the user is given the option fix values of θ and skip this loop in the optimization. Reactions were iterated in consecutive order to ensure adjustment to reactions occurring at higher temperatures did not affect the fit of prior reactions.

It was found that considering goodness of fit for the entire temperature domain of experimental data would dilute the programs ability to notice slight improvements, particularly for reactions with smaller MLR contributions and at the beginning of optimization. To account for this, the domain of data points considered by the goodness of fit metric begins as reaction-specific (considering only the data in the temperature domain immediately surrounding the current reaction peak), and gradually broadens as the program progresses until the entire experimental domain is considered. An example of the optimization program's progress from initial guess to optimized solution is shown in Figure 5.4.

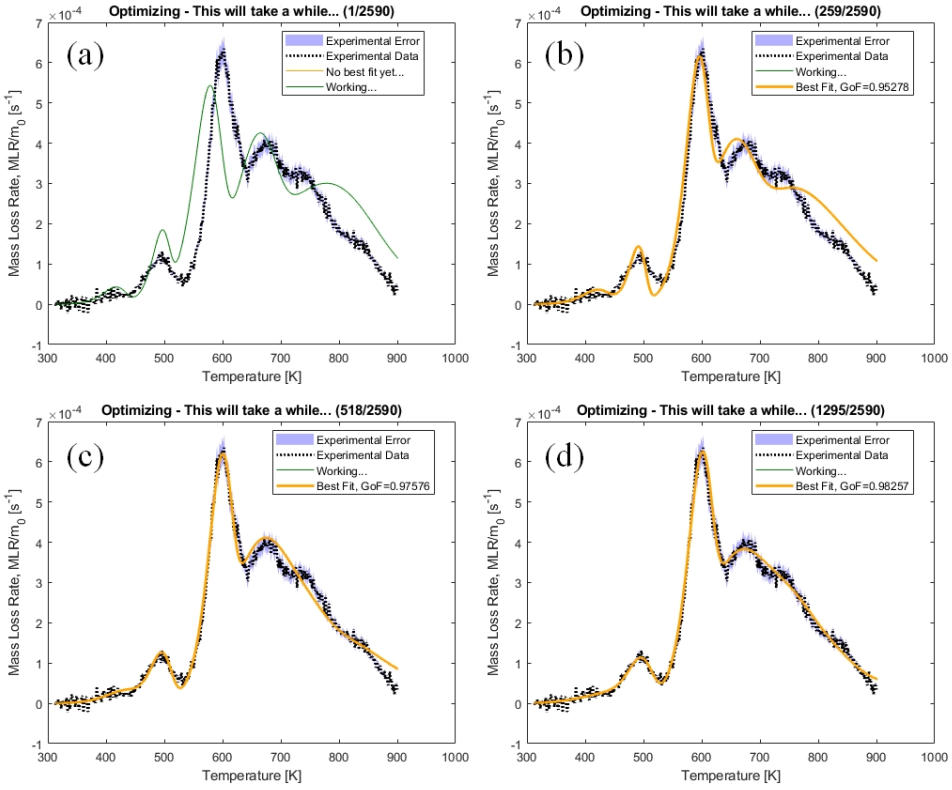

Figure 5.4: Example Foam Y optimization progress at initial guess (a), 1 complete cycle (b), 2 complete cycles (c), and optimized solution at 5 complete cycles (d). Convergence is determined shortly after 5 cycles.

For PMMA, optimization was performed using 10 K min^{-1} TGA data as a target. Results for each material are shown in Figure 5.5. The modeled curves agree well with the corresponding experimental data, achieving a GoF_M of 0.99 and 0.97 for extruded and cast, respectively. A summary of reaction mechanism and optimized parameters is provided in Table 5.1. Also tabulated here are heats of reactions, h, which are discussed in section 5.2.3. Most notable from these results is the quantitative differences in A and E between the two materials, the former of which varying by several orders of magnitude for the primary decomposition reaction. Also, both materials produce very small but detectable amount of final solid residue or char.

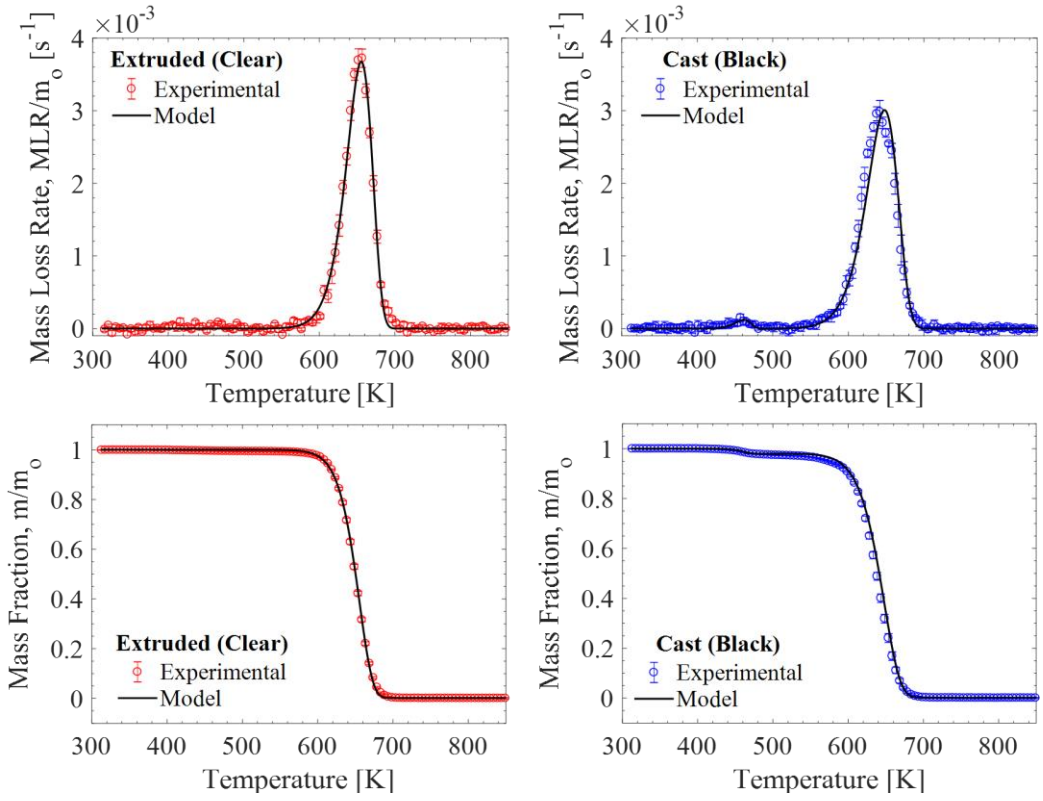

Figure 5.5: Model results vs. experimental for PMMA TGA simulations

Table 5.1: Summary of PMMA reaction stoichiometry, kinetics, and thermodynamics. Positive heat of reaction indicates endothermic reaction.

Rxn #	Reaction Equation	A (s^{-1})	E ($J \cdot mol^{-1}$)	h ($J \cdot kg^{-1}$)
	Extruded (Clear) PMMA			
1	$PMMA \rightarrow PMMA_{melt}$	*(glass transition)*		
2	$PMMA_{melt} \rightarrow 0.002\ CHAR + 0.998\ MMA_{gas}$	1.50×10^{14}	2.03×10^{5}	820×10^{3}
	Cast (Black) PMMA			
1	$PMMA \rightarrow PMMA_{melt}$	*(glass transition)*		
2	$PMMA_{melt} \rightarrow 0.98\ PMMA_{int} + 0.02\ MMA_{gas}$	4.95×10^{16}	1.64×10^{5}	5×10^{3}
3	$PMMA_{int} \rightarrow 0.002\ CHAR + 0.998\ MMA_{gas}$	1.35×10^{11}	1.64×10^{5}	817×10^{3}

For the more complex foam samples, optimization was performed using 10 K min^{-1} TGA data as a target. Results for each foam material are shown in Figure 5.6. It should be noted that for the final 2nd order reaction of Foam X, iterations were made directly to A and E because Equations (4) and (5) are only applicable to first order reactions. Results show very good agreement with experimental, achieving a GoF_M of 0.97 for both Foam X and Foam Y. The final residual yield is similar for both materials (34%) and is captured well. A summary of all reactions and optimized parameters is listed in Table 5.2.

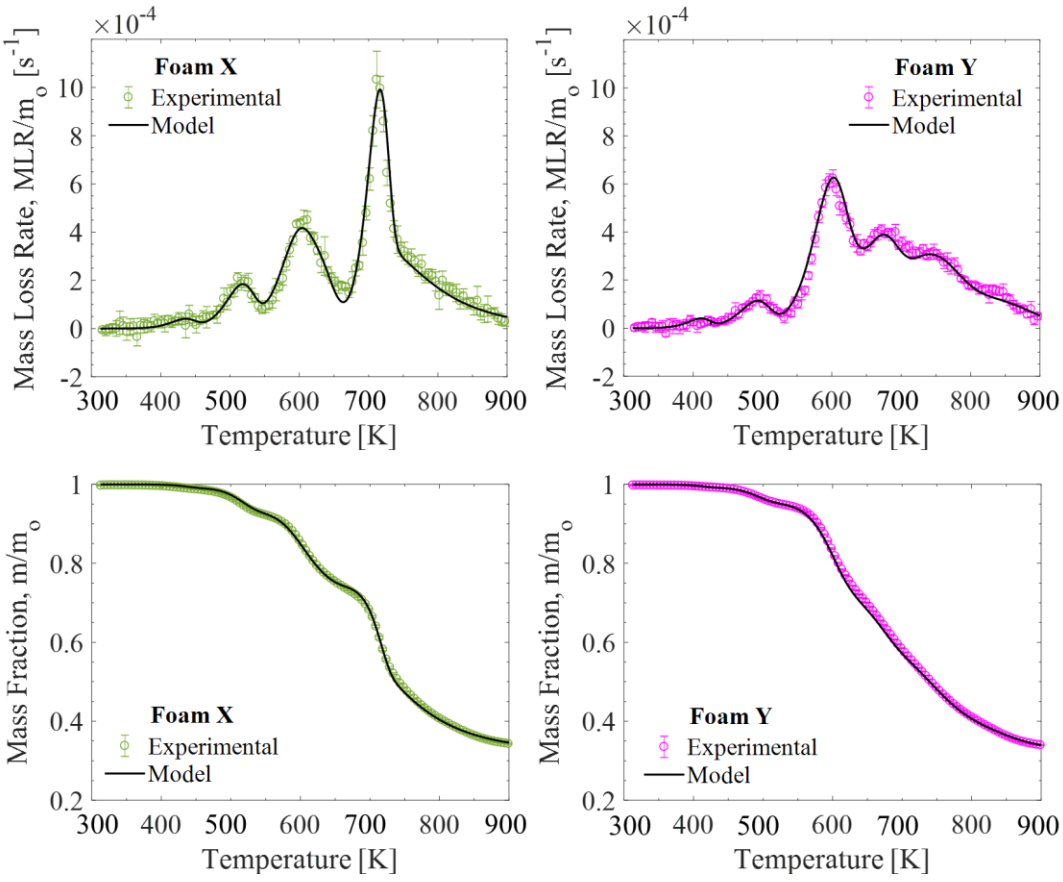

Figure 5.6: Model results vs. experimental for PIR foam TGA simulations.

Table 5.2: Summary of PIR foam reaction stoichiometry, kinetics, and thermodynamics. Positive heat of reaction indicates endothermic reaction.

Rxn #	Reaction Equation	A (s^{-1})	E ($J \cdot mol^{-1}$)	h ($J \cdot kg^{-1}$)
	Foam X			
1	FoamX → 0.0096 GAS_1 + 0.9904 INT_1	5.27×10^{7}	8.09×10^{4}	0
2	INT_1 → 0.061 GAS_2 + 0.939 INT_2	7.18×10^{8}	1.09×10^{5}	2.47×10^{4}
3	INT_2 → 0.097 GAS_3 + 0.903 INT_3	1.94×10^{9}	1.29×10^{5}	4.26×10^{4}
4	INT_3 → 0.13 GAS_4 + 0.87 INT_4	4.96×10^{6}	1.06×10^{5}	-7.26×10^{4}
5	INT_4 → 0.30 GAS_5 + 0.70 INT_5	1.33×10^{18}	2.75×10^{5}	3.93×10^{4}
6*	INT_5 + INT_5 → 0.90 GAS_6 + 1.1 CHAR	0.93×10^{0}	5.88×10^{4}	1.24×10^{5}
	Foam Y			
1	FoamY → 0.008 GAS_1 + 0.992 INT_1	2.42×10^{8}	8.09×10^{4}	0
2	INT_1 → 0.04 GAS_2 + 0.96 INT_2	2.27×10^{7}	8.95×10^{4}	2.16×10^{4}
3	INT_2 → 0.20 GAS_3 + 0.80 INT_3	5.62×10^{8}	1.24×10^{5}	2.51×10^{5}
4	INT_3 → 0.08 GAS_4 + 0.92 INT_4	1.00×10^{8}	1.20×10^{5}	-1.60×10^{5}
5	INT_4 → 0.17 GAS_5 + 0.83 INT_5	2.84×10^{7}	1.24×10^{5}	9.37×10^{3}
6	INT_5 → 0.29 GAS_6 + 0.71 INT_6	6.86×10^{3}	8.85×10^{4}	1.06×10^{5}
7	INT_6 → 0.27 GAS_7 + 0.73 CHAR	5.47×10^{1}	6.89×10^{4}	2.05×10^{5}

**Foam X Rxn #6 is a second-order reaction*

5.2.2 Manual Analysis: Thermodynamics of Decomposition

Upon determination of optimized kinetic and stoichiometric parameters defining the kinetic reaction mechanism, subsequent analysis shifted to inverse analysis of DSC data to determine the thermodynamics of decomposition. This inverse analysis is a two-step process: characterization of the heat capacities of each component followed by the heat of reaction associated with each reaction and transition. The numerical model associated with the heat flow to the sample in DSC simulations can be given as:

$$\frac{\dot{q}}{m_o} = \sum_{j=1}^{N_c} \frac{V}{m_o} \xi_j c_{p,j} \frac{\partial T}{\partial t} + \sum_{i=1}^{N_r} \frac{V}{m_o} r_i h_{r,i} \tag{8}$$

where $\dot{q}$ is the total heat flow, m_o is initial reactant mass, N_c and N_r are the number of components and reactants, respectively, V is the total sample volume, ξ_j and $c_{p,j}$ are the concentration and specific heat capacity of the j-th component, respectively, $\partial T/\partial t$ is the heating rate, and r_i and $h_{r,i}$ are the reaction rate and heat of reaction for the i-th reactant.

To determine the heat capacity of each component, a sensible enthalpy baseline is determined to isolate sensible enthalpy from the enthalpy associated with reactions and transitions. The sensible baseline is simulated within ThermaKin governed by Equation (8), where $h_{r,i}$ is set to 0 for every reaction, representing an absence of heat associated with chemical reactions and physical transitions in the reaction scheme. The resultant baseline is subsequently divided by the experimental heating rate to obtain the heat capacities of condensed phase materials as a function of temperature. This heat capacity vs. temperature profile combined with an intuition of the temperature domains that each component in a material exists allows for an approximation of the temperature-dependent heat capacity of each component. In many cases, the presence of reactions disrupts the heat capacity vs. temperature profile and assumptions must be made about the heat capacities of intermediate components. For the foam materials, repeat DSC experiments were conducted on the residual char yield for a more accurate measurement of the char component's temperature dependent heat capacity. All DSC analysis for the PIR foam samples was performed by Dushyant Chaudhari for his pending dissertation, and is presented here for completion [52].

For the PMMA materials, the heat capacity of the virgin material was determined by a linear fit of the heat capacity vs. temperature profile from 313 K to the glass transition. Similarly, the heat capacity of the $PMMA_{melt}$ component was determined by the linear fit between the glass transition and the onset of the primary decomposition reaction. For the cast PMMA, it was assumed that the heat capacity was not affected by the solvent reaction occurring

after the glass transition. For both materials, the char was assumed to have the same heat capacity as the melt material. The heat capacity of evolved gaseous species (MMA_{gas}) was set to be equal to 2000 J kg^{-1} K^{-1}, which corresponds to the average ideal gas heat capacity of the MMA monomer between 400 and 500 K [59]. Results of this analysis are shown in Table 5.3.

Table 5.3: Summary of PMMA component heat capacities

Component	c_p **(J** kg^{-1} K^{-1}**)**	**Component**	c_p **(J** kg^{-1} K^{-1}**)**
Extruded (Clear) PMMA		**Cast (Black) PMMA**	
PMMA	-2290 + 11.2T	PMMA	-1390 + 8.33T
$PMMA_{melt}$	1040 + 3.08T	$PMMA_{melt}$	850.5 + 3.07T
$PMMA_{char}$	1040 + 3.08T	$PMMA_{int}$	850.5 + 3.07T
		$PMMA_{char}$	850.5 + 3.07T
MMA_{gas}	2000	MMA_{gas}	2000

For the PIR foam samples, the heat capacity of the virgin material was defined as the linear (temperature dependent) fit of the heat capacity vs. temperature profile between 313 K and the onset of the first reaction, at 400 K. The heat capacity of the char was determined by performing separate DSC experiments consisting of solely the charred material and fitting a linear temperature dependency between 500-900 K for Foam X and 420-800 K for Foam Y. The heat capacities of intermediate components was prescribed to produce an experimental sensible heat flow baseline that provided good continuity with the fixed char heat flow at high temperatures. This was satisfied by prescribing the same heat capacity as the virgin material for Foam X, and a constant value (the virgin material's temperature dependent specific heat capacity evaluated at 420 K) for Foam Y. The heat capacity of all gaseous components was set to 2100 J kg^{-1} K, corresponding to the mean heat capacities of a gaseous C1 - C8 hydrocarbons at 600 K [60]. The heat capacity of the glass fiber component was gathered from results of Ding et al. [27]. Results are summarized in Table 5.4.

Table 5.4: Summary of PIR foam component heat capacities

Component	c_p **(J kg^{-1} K^{-1})**	**Component**	c_p **(J kg^{-1} K^{-1})**
Foam X		**Foam Y**	
FoamX	-113 + 3.94T	FoamY	-357.2 + 4.86T
INT_1	-113 + 3.94T	INT_1	1684
INT_2	-113 + 3.94T	INT_2	1684
INT_3	-113 + 3.94T	INT_3	1684
INT_4	-113 + 3.94T	INT_4	1684
INT_5	-113 + 3.94T	INT_5	1684
-	-	INT_6	1684
CHAR	722 + 0.110T	CHAR	883 + 0.411T
$GAS_{(1-6)}$	2100	$GAS_{(1-7)}$	2100
GF	442 + 1.24T	*GF*	442 + 1.24T

With heat capacities of each component determined, the remaining (second) term on the right-hand-side of Equation (8) is activated to determine the heat of each reaction and transition. An initial guess for $h_{r,i}$ for each reaction is made by subtracting the integral with respect to time of the sensible heat baseline from the integral of the experimental heat flow in the temperature domains corresponding to each reaction. An example of this integration is shown in Figure 5.7. The resultant values were subsequently adjusted manually until good agreement with experimental results was achieved. Criteria for agreement prioritized a good fit for the initial phases of the global reaction scheme and a good fit for Total Heat Flow (THF).

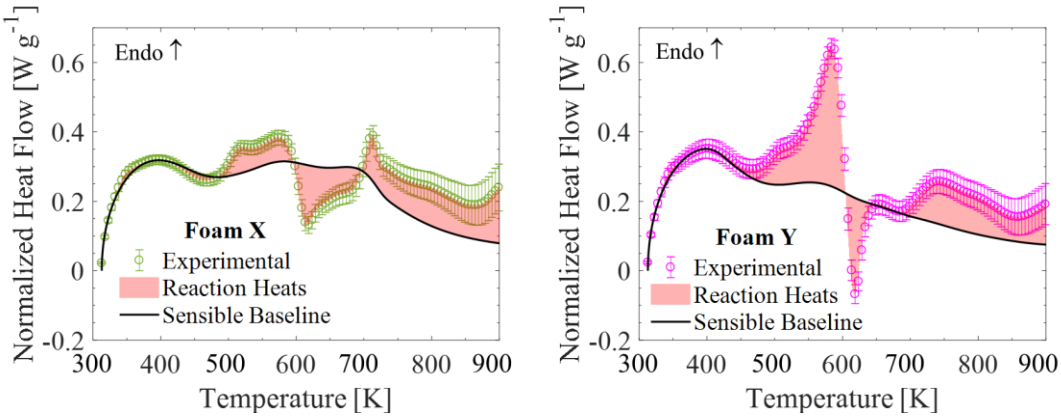

Figure 5.7: Simulated sensible heat baseline for PIR foam samples

For PMMA, analysis of heats of reaction was a straight forward integration with minor tuning because of the lack of overlapping reactions. Results of this analysis are summarized above in Table 5.1 and shown in Figure 5.8. Very good agreement is obtained for both PMMA materials.

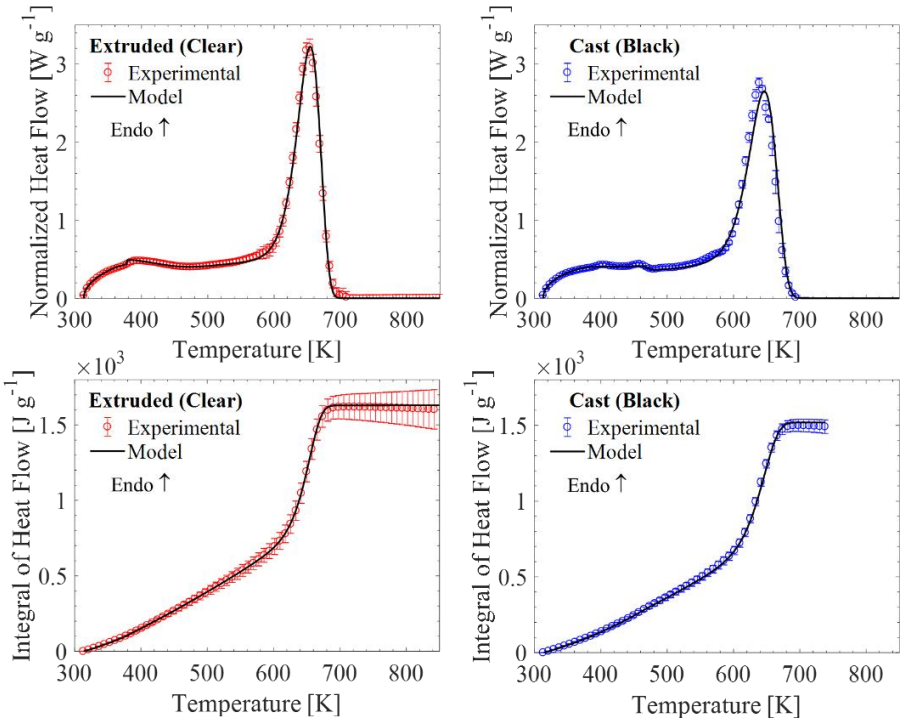

Figure 5.8: Simulated DSC results vs. experimental for PMMA

For the PIR Foam, analysis was more difficult because of the presence of overlapping reactions, requiring a number of manual iterations before an acceptable solution was sound. At higher temperatures, DSC uncertainty increases, so the fitting of lower temperature data was made a priority. Results are summarized above in Table 5.1 and shown in Figure 5.9. Results show acceptable agreement, with particularly good agreement for THR.

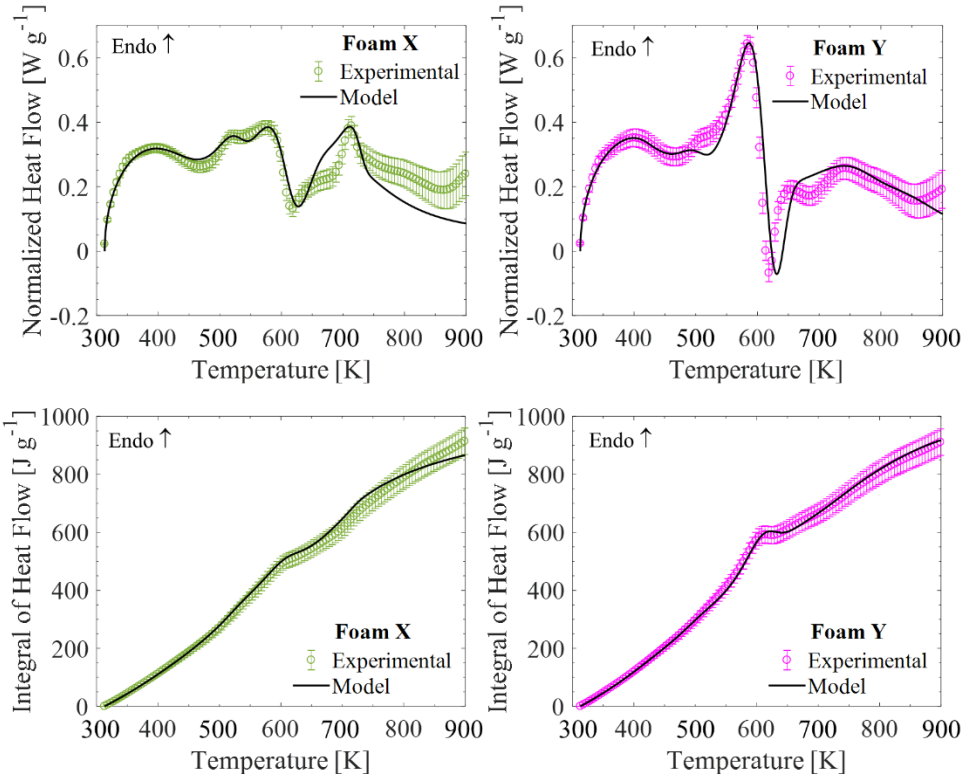

Figure 5.9: Simulated DSC results vs. experimental for PIR foam

5.2.3 Manual Analysis: Heat of Combustion

Heat release rate data from MCC experiments was manually inversely analyzed using ThermaKin simulations parameterized by well-defined MCC boundary conditions. The MLR attributed to evolved gaseous products from each reaction were independently multiplied by a

constant value representing heat of complete combustion according to a species-specific version of the common formulation of HRR:

$$HRR_{tot} = \sum_{i=1}^{N_c} \Delta H_{c,i} MLR_i \tag{9}$$

Where HRR_{tot} is the total heat release rate as comparable to MCC data, N_c is the total number of components involved in reactions, $\Delta H_{c,i}$ is the heat of combustion of the i-th gaseous component, and MLR_i is the temperature dependent MLR contribution of each i-th gaseous component. The value of total heat release (*THR*) is defined as the time integral of the heat release rate.

With the reaction kinetics well established from Section 5.2.1, inversely fitting the MCC experimental data becomes a task of assigning a single heat of combustion value to each gaseous decomposition product's MLR until modeled results show good agreement with experimental HRR. This iterative process is quite straightforward and can be done in a reasonable number of manual iterations. Analysis of heats of combustion for the foam samples was performed by Dushyant Chaudhari for his pending dissertation, and is presented here for completeness [52]. Results show good agreement, capturing peaks and total heat release well. Results are compiled in Table 5.5 and shown in Figure 5.10.

Table 5.5: Summary of complete heats of combustion for gaseous species

Component	ΔH_c (kJ g^{-1})	Component	ΔH_c (kJ g^{-1})
Foam X		**Foam Y**	
GAS_1	0	GAS_1	0
GAS_2	5	GAS_2	15
GAS_3	17	GAS_3	15
GAS_4	9	GAS_4	8
GAS_5	30	GAS_5	24
GAS_6	21	GAS_6	20
		GAS_7	33

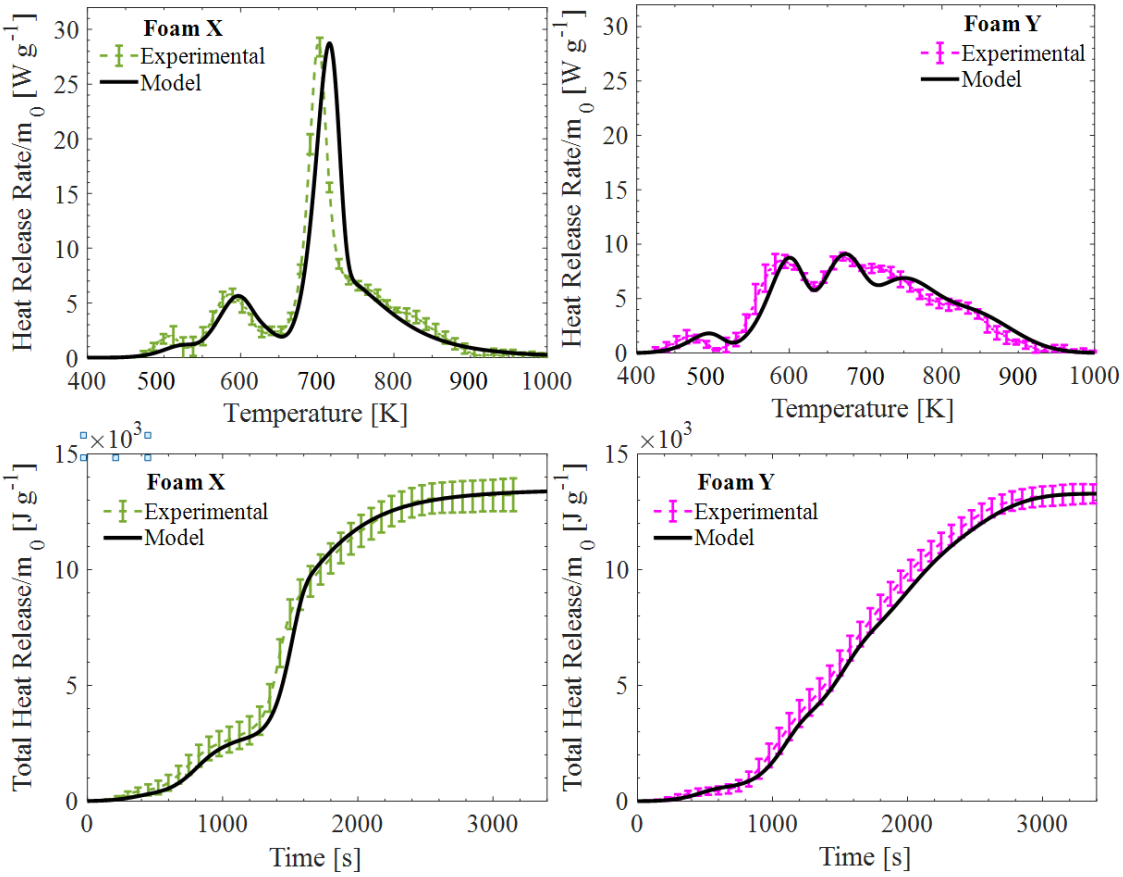

Figure 5.10: Simulated MCC results vs. experimental for PIR foam

For the PMMA samples, it is well documented that the decomposition scheme is dominated by the production of a single gaseous decomposition product, namely the monomer methyl methacrylate (MMA) [32]. Therefore, a direct integration of HRR resulted in heat of combustion for this single gaseous component. This method also retains the benefit of accumulating statistics for analysis of uncertainty. Uncertainties are small for this measurement representing a high degree of reproducibility. Results are summarized in Table 5.6.

Table 5.6: Heat of complete combustion for evolved gasses

Component	ΔH_c **(kJ g^{-1})**	**Component**	ΔH_c **(kJ g^{-1})**
Extruded (Clear) PMMA		**Cast (Black) PMMA**	
MMA_{gas}	24.33 ± 0.70	MMA_{gas}	24.05 ± 0.50

It should be noted that the initial solvent reaction (Reaction #2) observed in the TGA data for extruded PMMA is also observable in the HRR data (Figure 3.1), indicating that the gasified solvent has some heat associated with it. However, because the mass loss and heat production of Reaction 1 was too small to resolve (about 2% of the THR), so the same heat of combustion was assigned for the gaseous products of both reactions.

5.3 Gram-scale Analysis

With the kinetics and thermodynamics of thermal decomposition fully parameterized from milligram-scale analysis, the next step in the hierarchy of model development considers the contributing factors associated with mass transport properties, thermophysical properties (thermal conductivity and density), and optical properties (emissivity and absorption coefficient). The details of each analysis are as follows.

In this section of analysis, automated optimization was developed for parameterization of thermal conductivity and density. Optimization programs were developed for these

parameters to address the break in hierarchy of the model development process as a result of the interdependence and compensation effects between the two, similar to the compensation effects between A and E discussed in Section 5.2.1. In 1D numerical pyrolysis modeling, changes in density to individual components result in changes of thickness of the sample over time. When using back surface temperature of a thermally thick material as a target to parameterize the conduction through a sample, changes in density and thickness is closely coupled to the thermal conductivity, by association of Fourier's Law. Simultaneously capturing both the sample's thickness evolution and back surface temperature evolution presents a difficult iterative and labor intensive task. Therefore, automated programs were developed to optimize both density and thermal conductivity of each component in an attempt to resolve this interdependence, which is discussed in Sections 5.3.3 and 5.3.4.

5.3.1 Assumption: Mass Transport Properties

It has been qualitatively known that char developed from thermal degradation of polymers occasionally inhibits gaseous mass transport within the char matrix, but this effect is hard to experimentally measure [54]. As a simple first order approximation in this numerical framework, mass transport is prescribed such that gaseous mass leaves the material without restriction, with the option to introduce restrictions if results are insufficient. In the current study, this simplistic assumption was maintained as there was no evidence of restricted gas flow. The mass transport coefficient, λ, prescribed to each component is as follows.

For the non-charring PMMA, mass transport in/out of the condensed phase material was defined as sufficiently high ($\lambda = 2 \times 10^{-5}$ m^2 s^{-1}) for all components to ensure that mass associated with evolved gasses left the material immediately as to not cause artificial lag in the

MLR histories. The copper was set to be highly restrictive ($\lambda_{Cu} = 1 \times 10^{-30}$ m^2 s^{-1}) to gas flow to ensure gas did not diffuse through the copper foil substrate.

For the foam, special consideration was given to mass transport properties as a result of the increased thickness of the samples and presence of char. The mass transport in/out of the condensed phase material was defined as high ($\lambda = 2 \times 10^{-5}$ m^2 s^{-1}) for all material components except for the virgin material component and first intermediate component. The boundary mass transport in/out of the virgin material was shut down ($\lambda_{X,Y} = 1 \times 10^{-30}$ m^2 s^{-1}) to ensure that evolved gasses from upper layer decomposition did not travel backward into the virgin material, and were instead transported out of the system. Similarly, the mass transport in/out of the first intermediate material (INT_1) was defined as a weighted average of the virgin and evolved species ($\lambda_{INT1} = 2 \times 10^{-10}$ m^2 s^{-1}) to provide further resistance against gasses traveling back into undecomposed material. It was found that these changes in mass transport for the virgin and first intermediate components made only minute changes in MLR, manifesting only in the initial spike of MLR which became sharper and less smoothed as a result of gaseous mass leaving the system faster. The mass transport of the glass fiber material was set to be unrestrictive ($\lambda_{GF} = 2 \times 10^{-5}$ m^2 s^{-1}) and the copper was set to be highly restrictive ($\lambda_{Cu} = 1 \times 10^{-30}$ m^2 s^{-1}) to gas flow to maintain an impenetrable back boundary.

5.3.2 Direct Measurement: Radiative Properties

Radiative properties of each component of PMMA, namely absorption coefficient and emissivity, were prescribed according to measurements described in Section 2.3.2 and literature values, respectively. Linteris et al. [51] measured the radiative properties of both transparent and black PMMA using an integrating-sphere device and found the reflectivity (R_λ) of each to be approximately 0.04 for each material using samples of approximately 3mm thickness.

Emissivity is taken as $\varepsilon = 1 - R_\lambda$, or ε = 0.96 for each. The emissivities of the foam samples were approximated by comparative analysis of prescribed emissivity, as described later in this section.

Absorption coefficient was determined using experimental measurements and the generalized form of the Beer-Lambert Law from Equations (1) and (2), where surface emissivity, ε, is set to 0.96, and δ is measured to be 0.9×10^{-3} m. The results of this analysis is shown in Table 5.7. Experimental uncertainty of this measurement is large due to the inherent uncertainties of this setup during the brief 3 s of data acquisition. The uncertainty associated with the absorption coefficient normalized by density does not consider the propagation of density uncertainty. For input into ThermaKin, the absorption coefficient is normalized by component density, also shown in Table 5.7. These measurements were prescribed to every PMMA component, including the intermittent and char components.

Table 5.7: Optical properties of PMMA, shown in standard form and normalized by density.

Material	ε **(-)**	κ **(m^{-1})**	ρ **(kg·m^{-3})**	κ/ρ **(m^2·kg^{-1})**
Extruded (Clear) PMMA	0.96	1790 ± 150	1210 ± 30	1.47 ± 0.12
Cast (Black) PMMA	0.96	2870 ± 280	1210 ± 30	2.38 ± 0.23

For the foam samples, emissivity was approximated using comparative CAPA II experiments and defined emissivity paint (ε = 0.95). Additional CAPA II tests were performed where half of the sample was spray painted, as shown in Figure 5.11. The test was conducted at a nominal radiant flux of 70 kW m^{-2} and back surface temperature measurements were compared for each half (painted vs. unpainted) to determine whether the painting influenced the sample's optical properties. It was found that the paint made no notable difference for either foam during the period of majority of mass loss (~300 s), so it was assumed that all components

had an equivalent, constant emissivity of 0.95. Due to the porous surface of the foams, absorption coefficient was assumed to be 'high' (100 $m^2\ kg^{-1}$ = 3200 m^{-1}) and was adjusted to remain constant (3200 m^{-1}) despite changes in density. The evolution of density is described in Section 5.3.4. Results of optical properties and densities are summarized in Table 5.8.

Table 5.8: Optical properties of PIR foam; standard form and normalized by density.

Component	**ε (-)**	**κ (m^{-1})**	**ρ ($kg \cdot m^{-3}$)**	**κ/ρ ($m^2 \cdot kg^{-1}$)**
		Foam X		
FoamX	0.95	3200	32 ± 1	100
INT_1	0.95	3200	36.6	87
INT_2	0.95	3200	40.9	78
INT_3	0.95	3200	23.6	135
INT_4	0.95	3200	20.8	154
INT_5	0.95	3200	17.3	185
CHAR	0.95	3200	11.1	288
GF	*0.81*	*4160*	*2600*	*1.6*
		Foam Y		
FoamY	0.95	3200	32 ± 1	100
INT_1	0.95	3200	14.9	215
INT_2	0.95	3200	29.8	108
INT_3	0.95	3200	18.5	173
INT_4	0.95	3200	17.3	185
INT_5	0.95	3200	16.4	195
INT_6	0.95	3200	13.8	231
CHAR	0.95	3200	13.5	238
GF	*0.81*	*4160*	*2600*	*1.6*

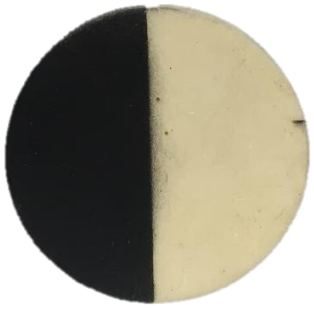

Figure 5.11: Exemplary half painted (ε=0.95) PIR foam sample for equivalent emissivity experiments

5.3.3 Optimization: Thermal Conductivity

The penultimate thermophysical property to determine in model development is thermal conductivity, *k*. CAPA II back surface temperature measurements were used as a target to parameterize thermal conductivity through inverse analysis. The boundary conditions of CAPA II experiments conducted in accordance with Section 2.3.2 were implemented into ThermaKin simulations as described previously (Section 4.2.2).

In the simplest, idealized case, thermal conductivity is effectively a constant value and independent of temperature. To comply with the objective of maintaining simplicity in model development, constant conductivity was preferred during model development; higher order temperature dependent terms were only to be activated when constant terms could not fully capture the heat transfer processes. The ThermaKin input scheme for thermal conductivity [W m^{-1} K^{-1}] defined by coefficients a, b, c and n is as shown in Equation (10).

$$\boldsymbol{k = a + bT + cT^{n}} \tag{10}$$

A hill climbing approach similar to TGA optimization was implemented, however, a new fitness function was defined:

$$GoF_T = 1 - \sqrt{\frac{\sum_{i=1}^{N}\left(\frac{Exp_i - Model_i}{Exp_i}\right)^2}{N}} \tag{11}$$

In this fitness function, the difference of squares in back surface temperature between experimental data (Exp_i) and model simulation ($Model_i$) is normalized by experimental temperature at each experimental point. The summation of these differences is normalized by the number of experimental data points, N. This target function prioritizes the fit of lower temperatures towards the beginning of the test over higher temperatures towards the end; this was chosen because lower temperatures represent conditions of onset of decomposition and are important for predicting ignition and fire spread. A perfect fit is marked by a GoF_T of 1. The domain of times and temperatures to be considered by the fitting target was selected by the user, with the default recommendation being the time domain associated with the first 80% of experimental mass loss. It was noticed towards the end of the PMMA CAPA II tests (after around 80% of expected mass loss), sample uniformity is compromised as thermal thickness becomes vague and uncertainty increases due to contributions of the epoxy. For the PIR foam samples, fitting was considered for the first 10 experimental minutes.

For each material component given a user cue to optimize, the program executes following hill climbing algorithm, outlined in the logic diagram shown in Figure 5.12. The GUI mentioned in the initialization steps allows configurable user input and is described in detail later in this section.

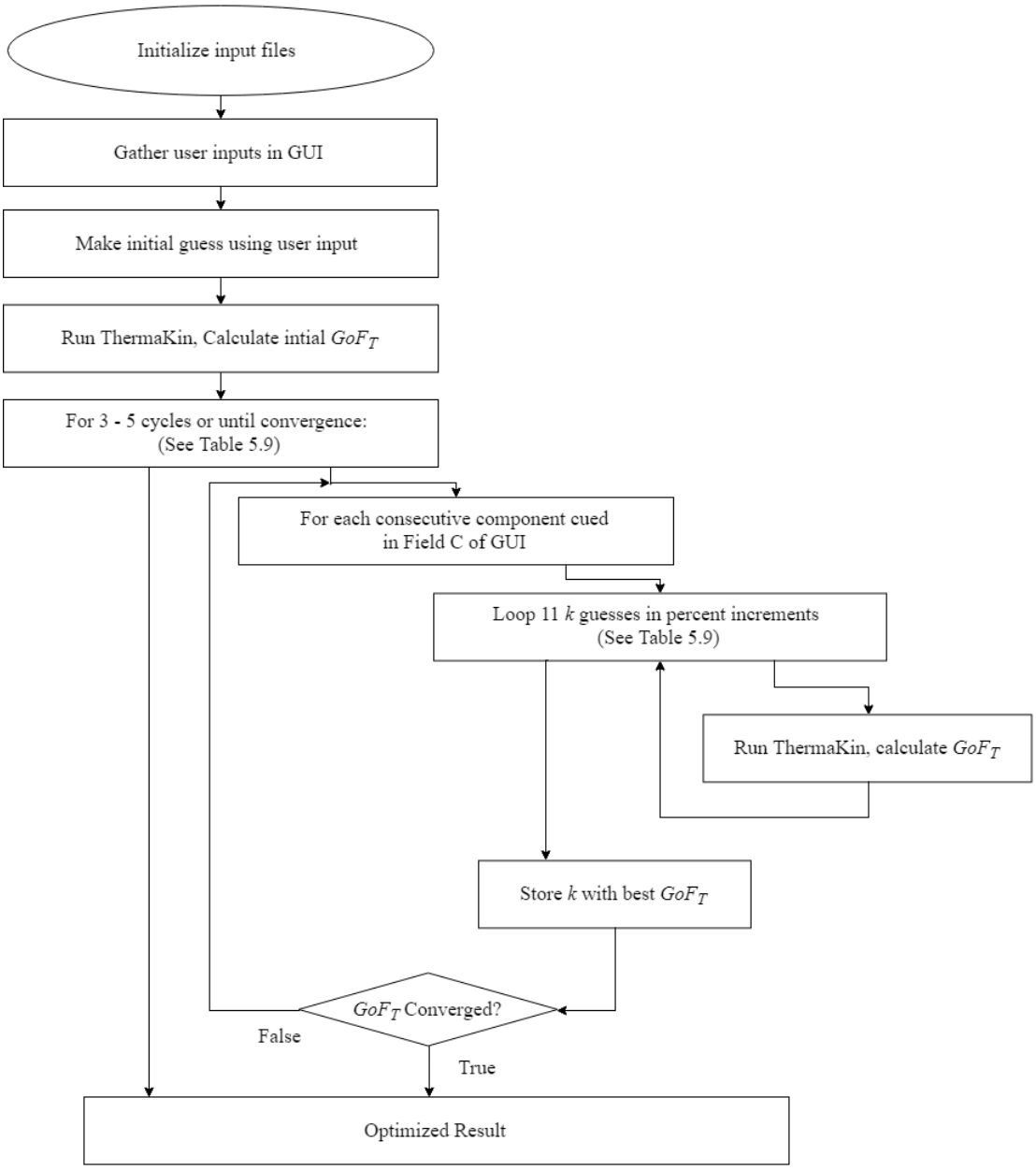

Figure 5.12: Logic diagram of program's algorithm for conductivity optimization

Optimization setup including user input was configured into a custom-built GUI is shown in Figure 5.13. Initial guesses of thermal conductivity for each component are inputted

(Field B) by the user based on intuition of the material in use. Field B is originally populated by the properties gathered from the input components file. The user is prompted with the option to create 'rules' to link component properties together in equivalency or user-defined proportions (Field E) to reduce dimensionality of the optimization and increase simplicity of the model. In addition, if initial conductivity was known from a manufacturer's spec sheet, or only certain components require optimization, an option was given to fix values to go unaltered by the optimizer (Field C). If the user does not provide an initial guess (cell value is 0) in Field B for a component checked as an optimizable parameter in Field C, initial guesses are automatically generated as 0.1, $1\times10^{-5}\times T$, or $1\times10^{-10}\times T^3$ [W m^{-1} K^{-1}] depending on whether the term coefficient is *a*, *b*, or *c*, respectively. Activating the C coefficient without manually inputting a corresponding *n* coefficient automatically forces the order of temperature dependence to $n = 3$.

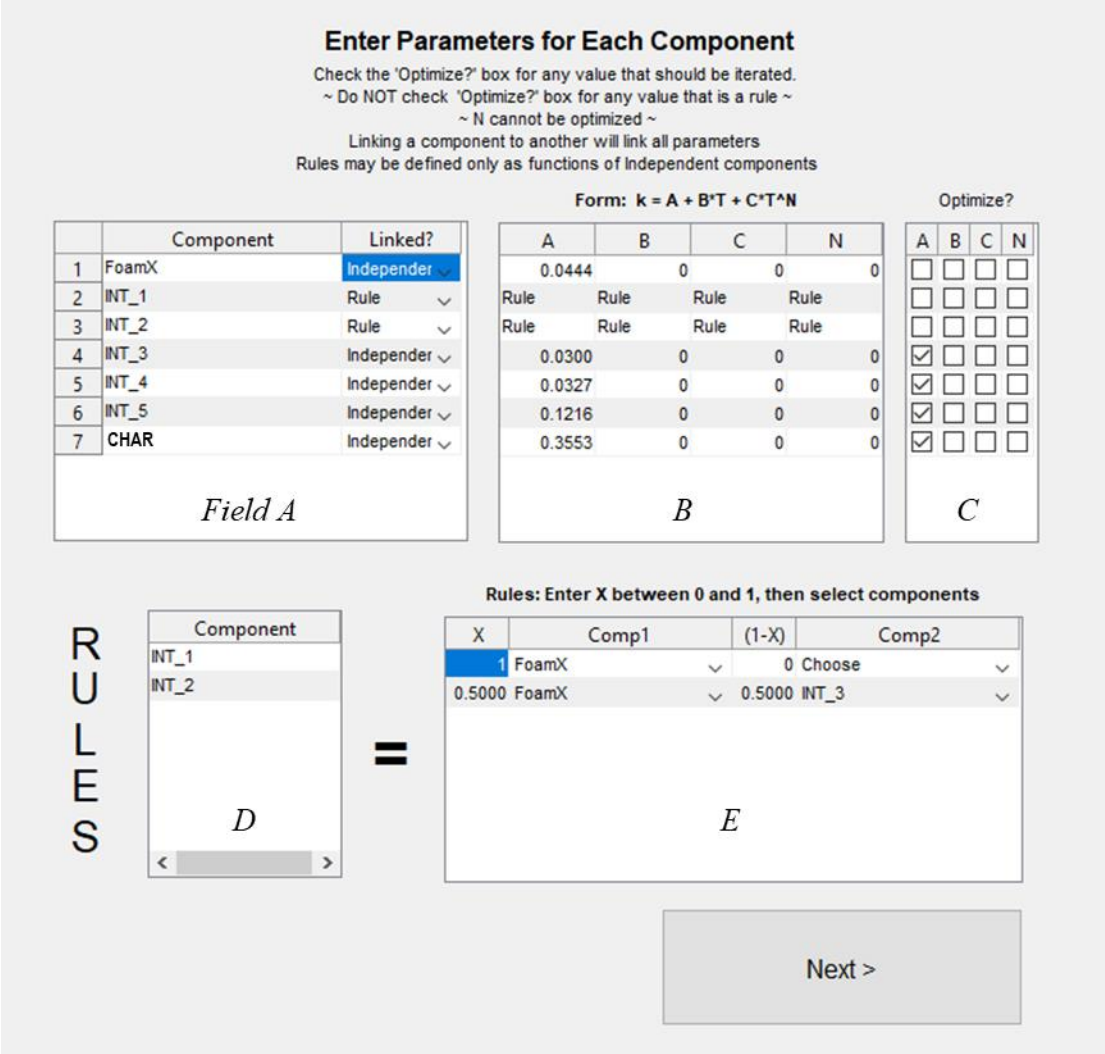

Figure 5.13: GUI for conductivity optimization initialization with labeled input fields

Lastly, the program offers user input to select ‘optimization resolution’ as ‘Coarse’, ‘Normal”, or ‘Fine’. This selection influences both the program’s selection of step size and the number of loops executed. The ‘Coarse’ mode will run approximately twice as many iterations as the ‘Fine’ mode with step sizes 3 times as large. This ‘Coarse’ mode is usually run with a ThermaKin conditions set with a reduced spatial and temporal resolution to prevent

exceptionally long run times. If the ‘Coarse’ mode is run on a high resolution ThermaKin conditions set, optimization could take several days on a typical desktop computer. Therefore, it is recommended to run a ‘Coarse’ or ‘Normal’ optimization with a low ThermaKin resolution, then fine tune the parameters using a ‘Fine’ optimization with full resolution ThermaKin simulations. The iterative step sizes for each mode are summarized in Table 5.9.

Table 5.9: Program parameters based on optimization resolution mode

Mode	Iterative Step Size per cycle	Number of Cycles	Total loops per component
‘Fine’	-16%,-8%,-4%,-2%,-1%,0%,1%,2%,4%,8%,16%	3	33
‘Normal’	-32%,-16%,-8%,-4%,-2%,0%,2%,4%,8%,16%,32%	4	44
‘Coarse’	-48%,-24%,-12%,-6%,-3%,0%,3%,6%,12%,24%,48%	5	55

An example of a ‘Course’ optimization run for a PIR foam starting from the default initial guess of 0.1 W m^{-1} K^{-1} is shown in Figure 5.14.

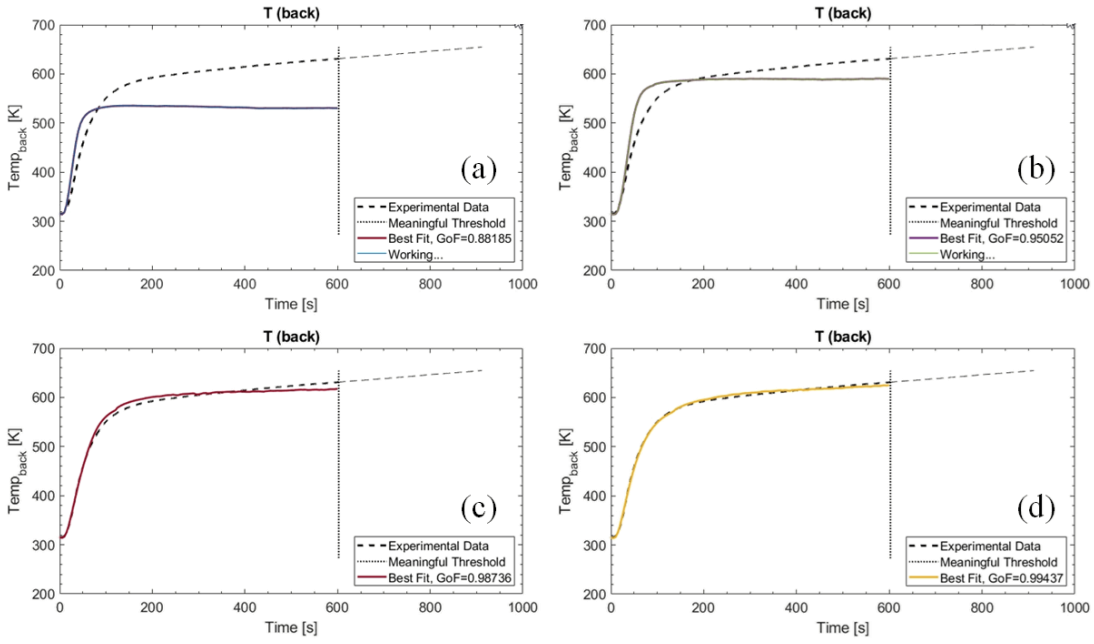

Figure 5.14: Example Foam X ‘Coarse’ optimization progress at initial guess (a), 1 complete cycle (b), 4 complete cycles (c), and optimized solution at 6 complete cycles (d).

In cases where higher order temperature dependent terms were activated, the hill climbing approach was still effective, separately making iterative steps to a, b, and/or c from Equation (10). This added complexity was activated by user cues of higher order terms in Field C of the GUI. The effectiveness of this approach on higher-order temperature dependent terms was directly related to the quality of the initial guess. In most cases, once the thermal conductivities had undergone preliminary optimization using only constant terms, a pseudo-temperature dependence could be determined based on intuition of the temperature ranges that each intermediate component exists. This pseudo-temperature dependence approximation provides insight sufficient for quality initial guesses. It was elected to not allow the program to automatically decide when to activate higher order temperature dependent terms in favor of preserving user intuition in the process.

For the PMMA, to comply with the objective of maintaining model simplicity, an attempt was made to optimize conductivity using only constant ($k = a$) terms. It was found that this implementation could not satisfactorally capture the back surface termperature evolution. Therefore, a temperature dependency was introduced, which is consistent with findings for this material in previous studies [25,31,61]. The program was tasked with optmizing a constant ($k = a$) condictivity term for the pre-glass transition material, and a temperature dependent ($k = a + bT$) conductivity for the post-glass transition material. The program used the 25 kW m^{-2} CAPA II back surface temperature data as a target, as experiments at this flux were better time resolved and maintained better sample uniformity. The residual yeild was sufficiently small such that it had marginal influence on the optimization, so char component was assumed to have the same conductivity as the glassy material. Optimization results produced a back surface temperature fit of GoF_T = 0.99 for both materials. Results are shown in Figure 5.15 and optimized conductivity values are summarized in Table 5.10.

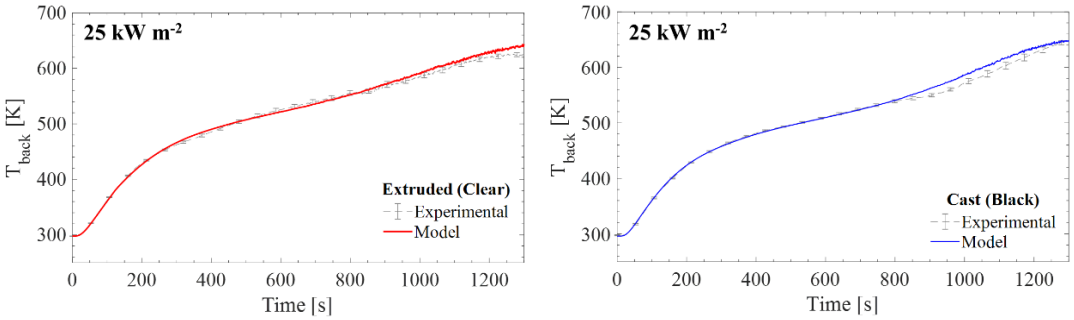

Figure 5.15: Results of PMMA thermal conductivity optimization vs. experimental.

Table 5.10: Summary of PMMA thermal conductivity

Component	***k* (W m^{-1} K^{-1})**	**Component**	***k* (W m^{-1} K^{-1})**
Extruded (Clear) PMMA		**Cast (Black) PMMA**	
PMMA	0.15	PMMA	0.16
$PMMA_{melt}$	0.34-0.00039*T*	$PMMA_{melt}$	0.34-0.00042*T*
CHAR	0.34-0.00039*T*	$PMMA_{int}$	0.34-0.00042*T*
		CHAR	0.34-0.00042*T*

For the foam materials, a previous study on PIR foam by Wang et al. [62] proposed a temperature dependent thermal conductivity model, finding that themal conduction within porous char strucutres is enhanced by raditiative heat tranport at high temperatures (> 500°C). It was found in this study that a pseudo-temperature dependence could be attained by varying constant conductivities throughout the multitude of components. Each component exists only in a specific temperature domain, thereby creating a piecewise function of contant conductivities corresponding to certain temperature ranges. This pseudo-temperature dependence produced by optimizing only constant conductivites for each intermediate component significantly reduces the dimensionality of the problem, and still produces good results. For the sake of model simplicity, it was accepted that the thermal conductivity for the

char component may be artificially high to compensate for the effect of radiant heat transport within the char pores. Therefore, the program was tasked with optimizing the system using only constant conductivity ($k = a$) terms using the 70 kW m^{-2} CAPA II back surface temperature data as a target. The 70 kW m^{-2} tests were chosen as a target because the 40 kW m^{-2} test samples were found to have not completely decomposed by the time tests were terminated. The initial guess for thermal conductivity was based on the room temperature conductivity advertised in the manufacturer's data sheet, and was applied to all components.

An initial 'Coarse' run with ThermaKin temporal and spatial resulution halved provided a prelimiary conductivity optimization that converges quickly. With these prelimiary results, the density was optimized (described next in Section 5.3.4) to ensure the material profile (thickness) evolution captured the evolution from experimetnal CAPA II tests. As noted in Section 5.3, the back surface temperature predictions are affected by changes in sample thickness as a result altering component densities, and the fit was slightly deteriorated as a result of the density optimization. The conductivity optimization was subsequently run a second time in the 'Fine' mode with full ThermaKin temporal and spatial resultion to converge on a solution. It was determined that this secondary optimization maintained a satisfactory profile evolution fit, and was therefore considered the final solution. The glass fiber component conductivity was not optimized by the program and was fixed to be consistent with prior findings [27]. The final optimized result is shown in Figure 5.16 and summarized in Table 5.11. Optimization results produced a back surface temperature fit of GoF_T = 0.99 for both materials.

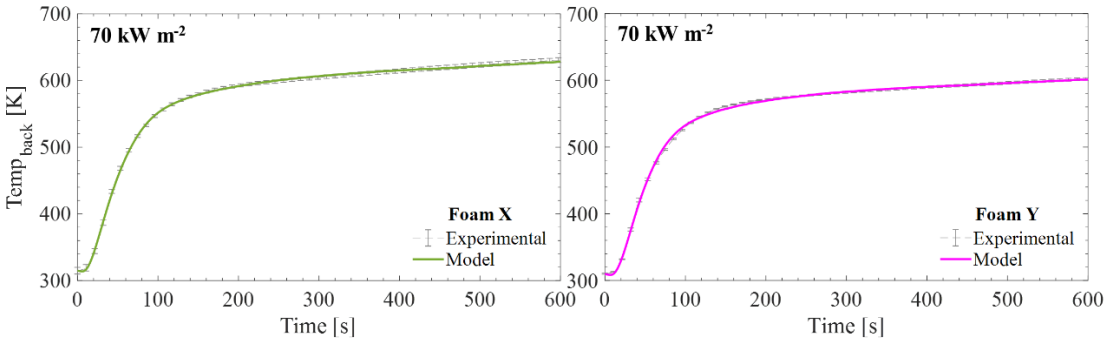

Figure 5.16: Results of PIR foam thermal conductivity optimization vs. experimental

Table 5.11: Summary of PIR foam thermal conductivity

Component	***k* (W m^{-1} K^{-1})**	**Component**	***k* (W m^{-1} K^{-1})**
Foam X		**Foam Y**	
FoamX	0.048	FoamY	0.046
INT_1	0.041	INT_1	0.092
INT_2	0.042	INT_2	0.040
INT_3	0.055	INT_3	0.078
INT_4	0.044	INT_4	0.061
INT_5	0.125	INT_5	0.140
CHAR	0.415	INT_6	0.151
		CHAR	0.252
GF	*0.36*	*GF*	*0.36*

Note: Thermal conductivity of glass fiber component was not optimized in algorithm

5.3.4 Optimization: Density

Profile (thickness) evolution describes changes in sample thickness during heating resulting from ablating and/or intumescent behavior. These behaviors can be simulated in ThermaKin by prescribing changes in density to intermediate components along the reaction scheme. Experimental profile evolution was monitored by the calibrated side view camera on

the CAPA II, and approximately measured by pixel distance post processing of these images. Analysis of the profile evolution was performed on the 70 kW m^{-2} tests, as these tests experienced the most pronounced changes in profile evolution.

PMMA ablates steadily and uniformly during thermal degradation, making its profile evolution a straightforward problem for numerical pyrolysis solvers. Accordingly, it was assumed that the density of every component in the decomposition scheme remained constant (1210 kg m^{-3}), and was independent of temperature. The mass accounting for the residual yield is negligibly small, so changes in the density of this char component were inconsequential.

PIR foam, conversely, has complex char structures and maintains nearly all of its thickness during thermal degradation. Foam Y experiences slight swelling during the first several seconds (~40 s) of heating, then slowly contracts for the rest of the test. Foam X shows no initial expansion, but shows contraction primarily at the beginning of heating. To account for these changes within the modeling framework, changes in density to intermediate components were made to correct for changes in volume (or thickness change, when considered in 1D simulation terms) during mass loss. An optimization routine based on a hill climbing algorithm was implemented to tune the density of each component until experimental profiles were matched. It was elected to describe each component's density using only constant terms independent of temperature because targeting profile evolution for inverse analysis provides only a very coarse first-order approximation of the density of each component. However, similar to the conductivity optimization, a pseudo temperature dependence is established by the piecewise nature of parameterizing a multitude of intermediate components.

As an initial guess, the density of each foam component was normalized by its stoichiometric mass coefficient for each step in the reaction scheme, starting from the measured density of the virgin sample. This implementation results in a simulation that maintains

constant volume (corresponding to constant thickness in 1D terms) during CAPA II simulations. The optimization program was built within an identical framework and algorithm to that of the thermal conductivity optimization program described Section 5.3.3. The density program implements the same hill climbing routine based on the same GoF_T criteria described in Section 5.3.3 and shown in Figure 5.12. Likewise, the density program features a GUI similar to the one shown in Figure 5.13 and described in in Section 5.3.3 which allows user input of initial guesses, designation of optimizable vs. fixed parameters, linking of components in specified proportions, and configurable temperature dependency of terms. Results of this density analysis are shown above in Table 5.8 within Section 5.3.2. As noted in Section 5.3.3, the conductivity optimization program was run a second time following the density optimization to converge on the final conductivity solution, which slight deteriorated the profile fit. This break of parameterization hierarchy was considered acceptable, as quality of profile evolution predictions were not as essential to the overall quality of the model compared to the thermal conductivity. After this readjustment, the resultant profile evolution still satisfactorily captured the experimental results, and was concluded to be the final result. This final profile is shown in Figure 5.17. In this figure, error is presented as $\pm 0.5 \times 10^{-3}$ m to account for significant variation in sample evolution due to uneven topography across the sample diameter.

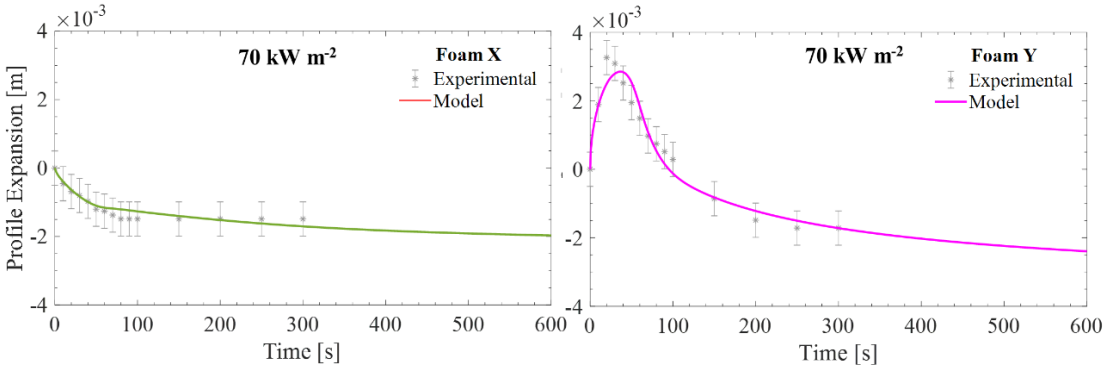

Figure 5.17: Profile evolution vs. experimental after final thermal conductivity optimization.

5.4 Efficiency

A benefit of these optimization algorithms is they do not require the computational power of a cluster and can be run on a typical PC. The optimizations in this study were run on a circa 2015 quad-core CPU (3.5 GHz) PC. Each optimization run only utilized a single core. Runs did not utilize parallel processing, but sometimes multiple optimization programs would be run simultaneously on the same CPU in different MATLAB windows. Runtimes were almost entirely dominated by the runtime of reach ThermaKin instance.

For the TGA optimization, during a full optimization of A, E, and θ (from initial guesses of A and E by Equations (4) and (5), and initial guess of θ automatically from TGA interpretation), individual ThermaKin iterations lasted only on the order of several seconds. For the PMMA, full optimizations approximated 15 and 30 minutes making 370 and 740 guesses for the single-reaction extruded and dual-reaction cast PMMA, respectively. For the PIR foam, full optimizations approximated 5 and 6.5 hours making 2220 and 2590 guesses for the 6-reaction Foam X and 7-reaction Foam Y, respectively.

For the thermal conductivity and density optimization, during full optimizations starting from initial guesses from manufacturer specs at room temperature, individual ThermaKin runs lasted on the order of several minutes. For the PMMA conductivity, full optimizations approximated 6 hours making 100 guesses for each extruded and cast PMMA, respectively. For the PIR foam, preliminary 'Coarse' mode runs for both conductivity and density optimization with low ThermaKin resolution could be run in 8 hours and provided good initial results ($GoF_T > 0.97$). Secondary 'Fine' mode conductivity optimization calling high resolution ThermaKin runs which lasted approximately 10 minutes each amounted to full optimization times of approximately 36 and 50 hours making 231 and 264 guesses for the 7-component, 6-reaction Foam X and 8-component, 7-reaction Foam Y, respectively.

The length of runtime and computational expense may be considered a drawback of these optimization programs in their current state. Runtimes, particularly for thermal conductivity optimization of complex decomposition schemes in a large domain, can run for several days, depending on the number of components in the reaction scheme, number of optimization loops, and resolution and number of elements of each ThermaKin instance. A user with limited knowledge or intuition for the sensitivity of each of these variables could easily initiate a run that could last weeks. However, while this runtime may be considered ‘long’, it is not prohibitive in the sense that the work would otherwise be longer and more labor intensive if done manually.

Chapter 6: Model Validation

The fully parameterized models were validated by assessing their ability to predict mass loss rate profiles from CAPA II experiments. These CAPA II MLR data were never used as a target during model parameterization and therefore may be considered as targets for validation. In addition, thermal transport properties were parameterized using back surface temperature data from a single CAPA heat flux, meaning the results from the alternate flux (60 kW m^{-2} for PMMA and 40 kW m^{-2} for foam) also serve as practical validation targets.

6.1 PMMA

The models developed for both PMMAs demonstrate good predictions of both back surface temperature and MLR profiles for the 60 kW m^{-2} tests. Model back surface temperatures closely follow experimental, with a particularly good accuracy during the beginning phases when temperature gradients are steepest. The back surface temperature profile begins to stray from experimental results towards the end of the test, which is likely a result of non-uniformity of sample thickness and impact of epoxy layer. The back surface temperature GoF_T calculated for the region corresponding to the first 80% of material mass loss is equal to 0.97 for both materials.

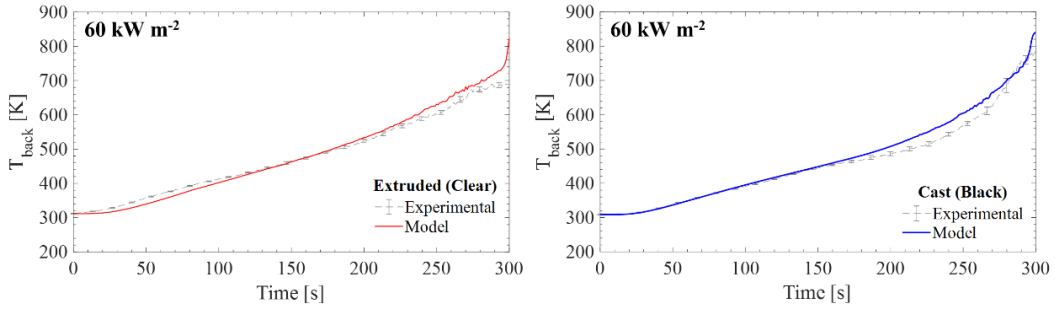

Figure 6.1: Independent predictions of back surface temperature from CAPA II experiments of PMMA.

Mass loss rates predictions at both heat fluxes show consistent results. Using the GoF_{MLR} metric from Equation (6) using only the MLR contribution ($\alpha = 1$), the fits were quantified as 0.91 and 0.94 for extruded and cast, respectively, for the 25 kW m^{-2} case. For the 60 kW m^{-2} case, the GoF_{MLR} was quantified as 0.86 and 0.91 for extruded and cast, respectively. The only systematic discrepancies observed are a slight underprediction of the onset of mass loss at the lower heat flux and a slight overprediction of the time to the maximum MLR at the higher heat flux. Despite these difference, these predictions serve as good validation of the model.

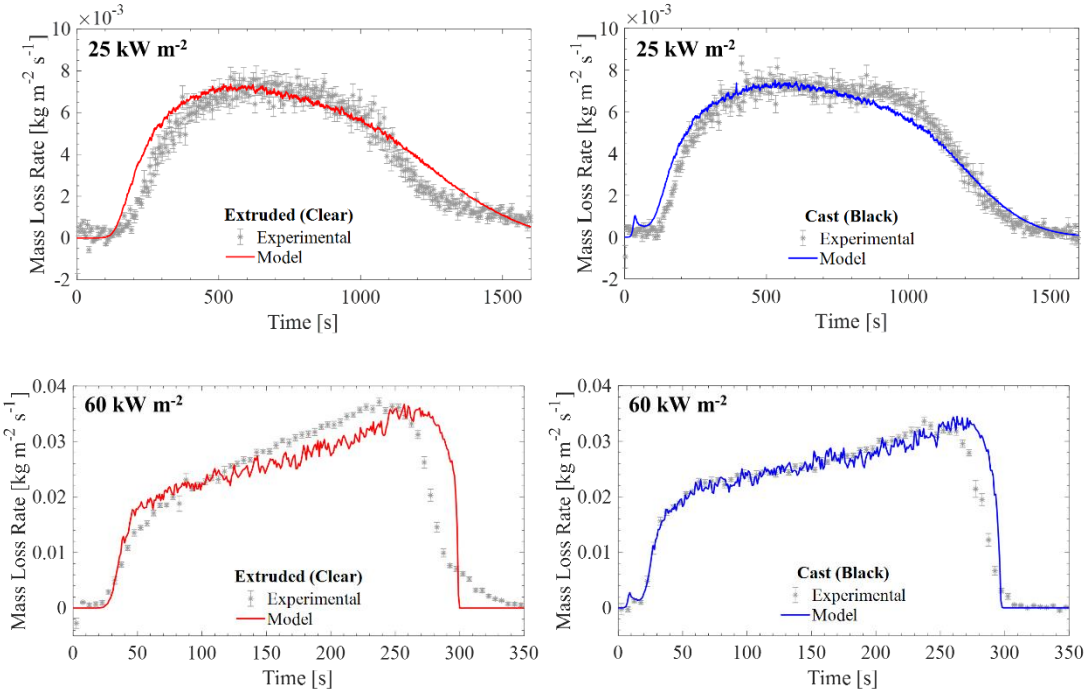

Figure 6.2: Independent predictions of MLR from CAPA experiments of PMMA.

6.2 PIR Foam

The models developed for both PIR foams demonstrate very good predictions of back surface temperature histories for the 40 kW m^{-2} CAPA II tests. The GoF_T of back surface temperature predictions calculated for the region corresponding to the first 600 s of mass loss is 0.97 for both foams. The only discrepancy is the slight overprediction at the very beginning of the tests.

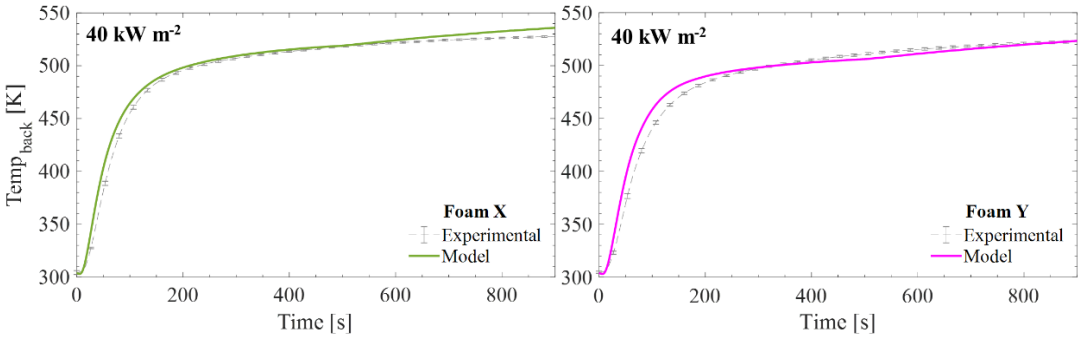

Figure 6.3: Independent predictions of back surface temperature from 40 kW m^{-2} CAPA II experiments of PIR foam

Mass evolution results, which are highly transient at the very beginning of the test, are shown as both MLR histories and mass fraction histories in Figure 6.4 and Figure 6.5. At the high flux (70 kW m^{-2}), the GoF_{MLR} corresponding to the first 600 s of mass loss is 0.90 and 0.91 for Foam X and Foam Y, respectively. The initial peak of MLR is captured well for both materials, but drops off more rapidly than experimental. This is compensated by the slight MLR overprediction between approximately 50 and 100 s. One notable discrepancy is the final mass fraction, analogous to residual char yield. This value was not captured well, possibly due to the model's missing mass loss associated with the release of the blowing agent within the pores, which as explained in Section 3.2, was not captured in the kinetics of decomposition. The

model is constrained by the residual yield parameterized from the TGA optimization and therefore will not produce a residual yield mass fraction below 0.34. This hypothesis does not fully explain the fact that this discrepancy of total mass loss is not observed in the final mass fraction of the 40 kW m^{-2} experiments (Figure 6.5). However, since the samples at 40 kW m^{-2} do not fully decompose and residual yield remains above 0.34, it is possible that some of the blowing agent is retained within the sample and is never released.

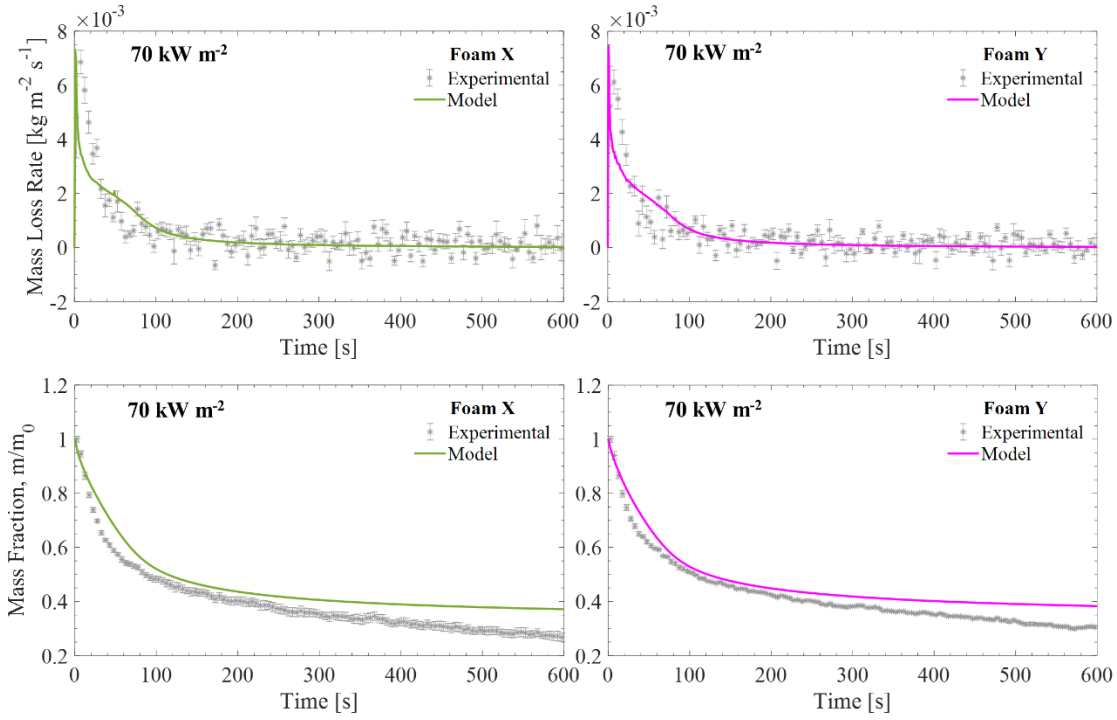

Figure 6.4: Independent predictions of MLR and Mass Fraction from 70 kW m^{-2} CAPA II experiments of PIR foam.

For the low flux tests (40 kW m^{-2}), similar phenomena is observed for MLR predictions, including a good prediction of initial mass loss rate, steep drop off causing underprediction, and then a brief region of overprediction, before leveling at a very small MLR value. GoF_{MLR} of MLR histories is 0.92 and 0.93 for Foam X and Foam Y, respectively; a slight improvement over the fit from the 70 kW m^{-2} MLR prediction. The final residual yield more

accurately predicts experimental results, particularly for Foam Y, as justified in the prior paragraph.

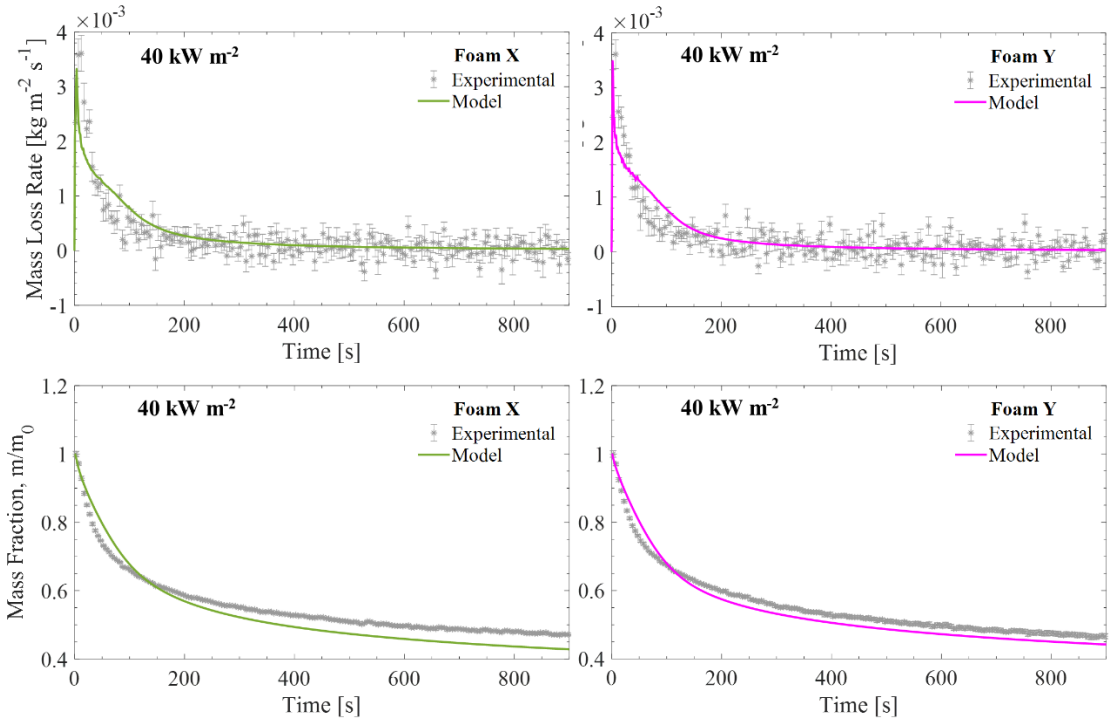

Figure 6.5: Independent predictions of MLR and Mass Fraction from 70 kW m^{-2} CAPA II experiments of PIR foam.

Chapter 7: Concluding Remarks

7.1 Conclusions

In this study, a well-established methodology for the development of comprehensive pyrolysis models is employed with the addition of optimization algorithms to automate three hierarchical steps in the development process. For two PMMA and two PIR rigid insulation foam materials, comprehensive pyrolysis models were developed based on an experimental dataset including milligram-scale experiments to define the kinetics and thermodynamics of thermal decomposition and gram-scale experiments to define and thermal transport and optical properties. PMMA and PIR foam represent two polymers with starkly different decomposition schemes that provide good test cases to evaluate the optimization algorithms' ability to resolve simple and complex materials. Modeling was handled by the ThermaKin numerical solver. The developed models have the ability to reproduce bench-scale experimental MLR profiles with good accuracy. Slight differences between the pairs of namely similar materials were well captured despite the overall similarity, suggesting the programs' have the ability to converge on unique solutions.

Milligram scale TGA tests were inversely analyzed in an automated fashion by looping instances of ThermaKin simulations within MATLAB as a subroutine. A new goodness of fit criteria similar to a coefficient of determination was established as the target function of the hill climbing algorithm. The novel feature of this algorithm is held in the iterative parameter space; rather than direct iterative guesses of A and E, iterations were made using physically derived expressions that calculate a unique pair of A and E, allowing for more intuitive steps sizes and direction during the implementation of the hill climbing algorithm. The program's run time was proportional to the number of reactions and the duration of ThermaKin

simulations, with very little overhead in between loops. Runs approximated 15 minutes for PMMA and 4 hours for foams on a typical PC and produced results that accurately capture experimental profile.

Optimization of thermal transport properties targeted the back surface temperature measurements from CAPA II experiments. The well-defined boundary conditions of CAPA II allow for isolation of thermal conductivity to be inversely analyzed in an automated fashion. A similar implementation to the prior algorithm was used, featuring looped instances of ThermaKin within MATLAB and a new goodness of fit criteria as the hill climbing target function. A GUI was built to improve functionality and usability to new users. Run times for this program were longer due to the increased complexity and duration of individual ThermaKin CAPA II runs (~10 minutes for each foam instance), with full optimization durations on the order of 6 hours for PMMA and 24+ hours for foam on a typical PC. A nearly identical algorithm performed successful optimization of component densities using profile (thickness) evolution as a target. These algorithms had comparable run times to the conductivity optimizations. Both algorithms produced very good agreement with their optimization targets for all materials tested.

These optimization algorithms show promising capability to streamline and improve the existing pyrolysis model development methodology. Automating the inverse analysis process presents a less labor intensive approach to manual parameterization which maintains physical and meaningful results with reduced compensation effects and achieves greater accuracy than manual analysis due to *GoF* criteria and multiplicity of guesses.

7.2 Efficiency

Computational efficiency and specific run times for each optimization program and each material were described in detail in Section 5.4. These algorithms feature great improvement in efficiency over the bulk optimization techniques described in chapter 1 (GA, GASA, SHC, SCE), which sometime require upwards of 100,000 iterative simulations on a computer cluster to converge on a solution. The algorithms in this study required a total of no more than 5,000 total iterative simulations to converge, granted that this number represents total iterations of 3 separate algorithms run in series. However, it is likely that any of these prior optimization algorithms would be as effective and efficient as the current algorithm if implemented into the framework and methodology of hierarchical experiments utilized in this study.

In general, on a typical modern PC, optimization of Arrhenius parameters can be performed overnight, and optimization of thermal conductivity and density (profile evolution) may last on the order of a day or two. Separated optimization runs can be run concurrently on the same machine in different MATLAB windows, as ThermaKin only utilizes a single CPU core. There is much room for improvements in terms of efficiency, but the current run times of the programs are not prohibitive considering the overall timeline of model development.

7.3 Drawbacks

While the optimization algorithm itself is universal and would be effective with any numerical pyrolysis modeling code, this study is specific to ThermaKin implementation. The program builds input files, passes the file to ThermaKin as an executable within MATLAB, then retrieves and interprets the ThermaKin output file, before processing the result and making decisions for the next iteration. If this algorithm were to be implemented with another pyrolysis

model, such as Gpyro or the condensed phase sub model in the Fire Dynamics Simulator (FDS), a new framework would have to be built to accommodate the program's input and output file types and syntax. However, Gpyro is already implemented into MATLAB, so this compatibly framework should not be highly difficult.

7.4 Future Work

Based on the results of the present study, future work could be done to further the capability and efficiency of these optimization algorithms. However, work should proceed with caution as to be careful to not remove too much user intervention and accountability in an effort to maintain physicality and meaning to results. Therefore, developments should focus primarily on the efficiency and accuracy of current implementations. In general, efforts to add further intelligence into initial guesses or the decision making process in selecting step size and direction could vastly improve computational time. Also, better convergence criteria (possibly based on gradient-based analysis of *GoF* evolution) could reduce computational time by reducing iterations that only make fine-tuned changes with greater precision than are reportable significant digits. The introduction of stochastic guessing may also improve the program's ability to avoid local maxima. Furthermore, logic could be implemented to programmatically decide or recommend when to activate higher-order temperature dependence of properties.

The implementation of parallel processing could also vastly improve computational efficiency, particularly for the thermal conductivity optimization. Currently, all instances are computed consecutively; that is, each ThermaKin run is run and to completion processed before the next run is considered (i.e., run in series). In the current steepest ascent hill climbing framework, parallel processing could be both effective and rather simple to implement considering a step is not chosen until approximately a dozen guesses have been run and

processed. The number of parallel processes would be limited by MATLAB as the number of available cores, with a current (MATLAB version R2019a) maximum limit of 12.

For further verification of the optimization program's ability to accurately parameterize material properties, more tests on various unique materials should be considered. For validation of the programs' ability to find a unique, global solution (thus implying a good resistance to compensation effects), the algorithms should be tested against manufactured data of known input parameters.

Lastly, a technique within the framework of the reaction kinetics optimization could be extended to optimize the heats of reaction from DSC tests and heats of combustion from MCC tests, which are currently performed manually. Implementing these two analyses in an automated fashion would additionally improve accuracy and speed of the parameterization process, but to a lesser extent than the improvements made by the programs presented in this study. In theory, a single program could be capable of performing every step of the present parameterization process (including all current manual steps) with no user intervention except for input of all experimental data. This would still be distinct from a massively parallel optimizations described in the introduction, as this would be several distinct programs running isolated optimization routines in a hierarchical series. However, caution should be considered when proceeding with further automation to ensure the overall model development process does not become detached from physical understanding and physical meaning.

Appendix I: Summary of Material Properties

Extruded (Clear) PMMA

Component	**ρ**	**ε**	**κ**	**κ**	**k**	**λ**	**c_p**	**ΔH_C**
	kg m^{-3}	-	kg m^{-2}	m^{-1}	W m^{-1} K^{-1}	m^2 s^{-1}	J kg^{-1} K^{-1}	kJ kg^{-1}
PMMA	1210	0.96	1790	1.47	0.15	2.00E-05	-2292 + 11.24*T*	-
$PMMA_{melt}$	1210	0.96	1790	1.47	0.34 -0.00039*T*	2.00E-05	1039 + 3.082*T*	-
CHAR	1210	0.96	1790	1.47	0.34 -0.00039*T*	2.00E-05	1039 + 3.082*T*	-
MMA_{gas}	1210	0.96	1790	1.47	0.34 -0.00039*T*	2.00E-05	1800	24330

Reaction								**A**	**E**	***θ***	**h_r***
								s^{-1}	J·mol^{-1}	(solid)	J·kg^{-1}
1	PMMA	+	NOCOMP	->	$PMMA_{melt}$	+	NOCOMP	1	0	1	0
2	$PMMA_{melt}$	+	NOCOMP	->	CHAR	+	MMA_{gas}	1.5E+14	2.03E+05	0.001825	-8.20E+05

**Negative h_r values indicate endotherm*

Cast (Black) PMMA

Component	**ρ**	**ε**	**κ**	**κ**	**k**	**λ**	**c_p**	**ΔH_c**
	kg m^{-3}	-	kg m^{-2}	m^{-1}	W m^{-1} K^{-1}	m^2 s^{-1}	J kg^{-1} K^{-1}	kJ kg^{-1}
$PMMA_{black}$	1210	0.96	2870	2.38	0.16	2.00E-05	-1391 + 8.329*T*	-
$PMMA_{melt}$	1210	0.96	2870	2.38	0.34 – 0.00042*T*	2.00E-05	850.5 + 3.072*T*	-
$PMMA_{int}$	1210	0.96	2870	2.38	0.34 – 0.00042*T*	2.00E-05	850.5 + 3.072*T*	-
CHAR	1210	0.96	2870	2.38	0.34 – 0.00042*T*	2.00E-05	850.5 + 3.072*T*	-
MMA_{gas}	1210	0.96	2870	2.38	0.34 – 0.00042*T*	2.00E-05	850.5 + 3.072*T*	24050

Reaction								**A**	**E**	***θ***	**h_r***
								s^{-1}	J·mol^{-1}	(solid)	J·kg^{-1}
1	$PMMA_{black}$	+	NOCOMP	->	$PMMA_{melt}$	+	NOCOMP	1	0	1	0
2	$PMMA_{melt}$	+	NOCOMP	->	$PMMA_{int}$	+	MMA_{gas}	4.95E+16	163680	0.98	-5000
3	$PMMA_{int}$	+	NOCOMP	->	CHAR	+	MMA_{gas}	1.35E+11	164155.2	0.00204	-8.17E+05

**Negative h_r values indicate endotherm*

Foam X

Component	**ρ**	**ε**	**κ**	**κ**	**k**	**λ**	**c_p**	**ΔH_C**
	kg m^{-3}	-	kg m^{-2}	m^{-1}	W m^{-1} K^{-1}	m^2 s^{-1}	J kg^{-1} K^{-1}	kJ g^{-1}
Foam X	32	0.95	100	3200	0.0481	1.00E-30	-112.8 + 3.936*T*	-
Int1	36.6	0.95	87	3200	0.0408	2.00E-10	-112.8 + 3.936*T*	-
Int2	40.9	0.95	78	3200	0.0419	2.00E-05	-112.8 + 3.936*T*	-
Int3	23.6	0.95	135	3200	0.0548	2.00E-05	-112.8 + 3.936*T*	-
Int4	20.8	0.95	154	3200	0.0437	2.00E-05	-112.8 + 3.936*T*	-
Int5	17.3	0.95	185	3200	0.1247	2.00E-05	-112.8 + 3.936*T*	-
CHAR	11.1	0.95	288	3200	0.4154	2.00E-05	721.5 + 0.1097*T*	-
GF	2600	0.81	1.6	4160	0.36	2.00E-05	442 + 1.24*T*	-
Gas1	36.6	0.95	87	3200	0.0408	2.00E-05	2100	0
Gas2	40.9	0.95	78	3200	0.0419	2.00E-05	2100	5
Gas3	23.6	0.95	135	3200	0.0548	2.00E-05	2100	17
Gas4	20.8	0.95	154	3200	0.0437	2.00E-05	2100	9
Gas5	17.3	0.95	185	3200	0.1247	2.00E-05	2100	30
Gas6	11.1	0.95	288	3200	0.4154	2.00E-05	2100	21

Reaction									**A**	**E**	***θ***	**h_r***
									s^{-1}	J·mol^{-1}	(solid)	J·kg^{-1}
1	FoamX	+	NOCOMP	->	GAS_1	+	INT_1		5.27E+07	8.09E+04	0.9904	0
2	INT_1	+	NOCOMP	->	GAS_2	+	INT_2		7.18E+08	1.09E+05	0.939	-2.47E+04
3	INT_2	+	NOCOMP	->	GAS_3	+	INT_3		1.94E+09	1.29E+05	0.903	-4.26E+04
4	INT_3	+	NOCOMP	->	GAS_4	+	INT_4		4.96E+06	1.06E+05	0.87	7.26E+04
5	INT_4	+	NOCOMP	->	GAS_5	+	INT_5		1.33E+18	2.75E+05	0.7	-3.93E+04
6	INT_5	+	INT_5	->	GAS_6	+	CHAR		0.925	5.88E+04	1.1	-1.24E+05

**Negative h_r values indicate endotherm*

Foam Y

Component	**ρ**	**ε**	**κ**	**κ**	**k**	**λ**	**c_p**	**ΔH_c**
	kg m^{-3}	-	kg m^{-2}	m^{-1}	W m^{-1} K^{-1}	m^2 s^{-1}	J kg^{-1} K^{-1}	kJ g^{-1}
Foam Y	32	0.95	100	3200	0.046	1.00E-30	-357.2 + 4.86*T*	-
Int1	14.9	0.95	215	3200	0.092	2.00E-10	1684	-
Int2	29.8	0.95	108	3200	0.040	2.00E-05	1684	-
Int3	18.5	0.95	173	3200	0.078	2.00E-05	1684	-
Int4	17.3	0.95	185	3200	0.061	2.00E-05	1684	-
Int5	16.4	0.95	195	3200	0.140	2.00E-05	1684	-
Int6	13.8	0.95	231	3200	0.151	2.00E-05	1684	-
CHAR	13.5	0.95	238	3200	0.252	2.00E-05	883 + 0.411*T*	-
GF	2600	0.81	1.6	4160	0.36	2.00E-05	442 + 1.24*T*	-
Gas1	14.9	0.95	215	3200	0.092	2.00E-05	2100	0
Gas2	29.8	0.95	108	3200	0.040	2.00E-05	2100	15
Gas3	18.5	0.95	173	3200	0.078	2.00E-05	2100	15
Gas4	17.3	0.95	185	3200	0.061	2.00E-05	2100	8
Gas5	16.4	0.95	195	3200	0.140	2.00E-05	2100	24
Gas6	13.8	0.95	231	3200	0.151	2.00E-05	2100	20
Gas7	13.5	0.95	238	3200	0.252	2.00E-05	2100	33

Reaction								**A**	**E**	***θ***	**h_r***
								s^{-1}	J·mol^{-1}	(solid)	J·kg^{-1}
1	FoamX	+	NOCOMP	->	GAS_1	+	INT_1	5.27E+07	8.09E+04	0.9904	0
2	INT_1	+	NOCOMP	->	GAS_2	+	INT_2	7.18E+08	1.09E+05	0.939	-2.47E+04
3	INT_2	+	NOCOMP	->	GAS_3	+	INT_3	1.94E+09	1.29E+05	0.903	-4.26E+04
4	INT_3	+	NOCOMP	->	GAS_4	+	INT_4	4.96E+06	1.06E+05	0.87	7.26E+04
5	INT_4	+	NOCOMP	->	GAS_5	+	INT_5	1.33E+18	2.75E+05	0.7	-3.93E+04
6	INT_5	+	INT_5	->	GAS_6	+	CHAR	0.925	5.88E+04	1.1	-1.24E+05

**Negative h_r values indicate endotherm*

Appendix II: Example ThemaKin Input Files

Components Input: Extruded PMMA

```
COMPONENT:      PMMA
STATE:          S
DENSITY:        1210  0  0  0
HEAT CAPACITY:  -2292  11.24  0  0
CONDUCTIVITY:   0.15        0        0        0
TRANSPORT:      2e-5  0  0  0
EMISSIVITY & ABSORPTION:  0.96  1.47

COMPONENT:      PMMA_glass
STATE:          S
DENSITY:        1210  0  0  0
HEAT CAPACITY:  1039  3.082  0  0
CONDUCTIVITY:   0.34   -0.00039        0        0
TRANSPORT:      2e-5  0  0  0
EMISSIVITY & ABSORPTION:  0.96  1.47

COMPONENT:      CHAR
STATE:          S
DENSITY:        1210  0  0  0
HEAT CAPACITY:  1039  3.082  0  0
CONDUCTIVITY:   0.34   -0.00039        0        0
TRANSPORT:      2e-5  0  0  0
EMISSIVITY & ABSORPTION:  0.96  1.47

COMPONENT:      MMA
STATE:          G
DENSITY:        1210  0  0  0
HEAT CAPACITY:  1800  0  0  0
CONDUCTIVITY:   0.34   -0.00039        0        0
TRANSPORT:      2e-5  0  0  0
EMISSIVITY & ABSORPTION:  0.96  1.47

COMPONENT:      COPPER
STATE:          S
DENSITY:            8933        0        0        0
HEAT CAPACITY:  385         0        0        0
CONDUCTIVITY:   401         0        0        0
TRANSPORT:      1e-30   0        0        0
EMISSIVITY & ABSORPTION:            0.95        10000

MIXTURES
S SWELLING:         0
L SWELLING:         0
G SWELLING LIMIT:   1e-30
PARALL CONDUCTIVITY:  0.5
PARALL TRANSPORT:     0.5

REACTION:       PMMA + NOCOMP -> PMMA_glass + NOCOMP
STOICHIOMETRY:  1    0        1    0
ARRHENIUS:      1  0
HEAT:           0  0  0  0
TEMP LIMIT:     L  378

REACTION:       PMMA_glass + NOCOMP -> CHAR + MMA
STOICHIOMETRY:  1 0 0.00182 0.99818
ARRHENIUS:      1.5e4 2.03e5
HEAT:           -820000  0  0  0
TEMP LIMIT:     L  300
```

Component state is a solid (S), liquid (L) or gas (G).

Component properties have 4 numbers corresponding to coefficients in following input format:

$$p = p_0 + p_1 T + p_2 T^n$$

Properties are defined in SI units, namely kg m^{-3} for density, J kg^{-1} K^{-1} f heat capacity, W m^{-1} K^{-1} for thermal conductivity, and m^2 s^{-1} for gas transfer coefficient (TRANSPORT)

Component emissivity is dimensionless, and absorption coefficient is normalized by component density (m^2 kg^{-1})

Default dimensionless parameters specifying reaction of material volume to the presence of gases. See [2]

Default dimensionless parameters for calculation of thermal conductivity and gas transfer for mixtures. See [2]

Reaction stoichiometry is limited to 2 components per side. NOCOMP indicates reaction doesn't have second reactant or product. First order reactions shown here. A second order reaction would read:

PMMA + PMMA -> PMMA_glass + NOCOMP

Indicates lower (L) temperature limit [K] which reaction can be activated. Used in conjunction with A= 1 s^{-1} and E= 0 to define a fast transition, such as this glass transition at 378K. The reverse can be prescribed with an upper (U) temperature limit.

Stoichiometric coefficients for the 4 reaction components in the line above

Pre-exponential factor [s^{-1} or m^3 kg^{-1} s^{-1}], and Activation energy [J mol^{-1}]

Heat of reaction [J kg^{-1}]. Negative value indicates endotherm.

Conditions Input: PMMA CAPA II test at 60 kW m^{-2}

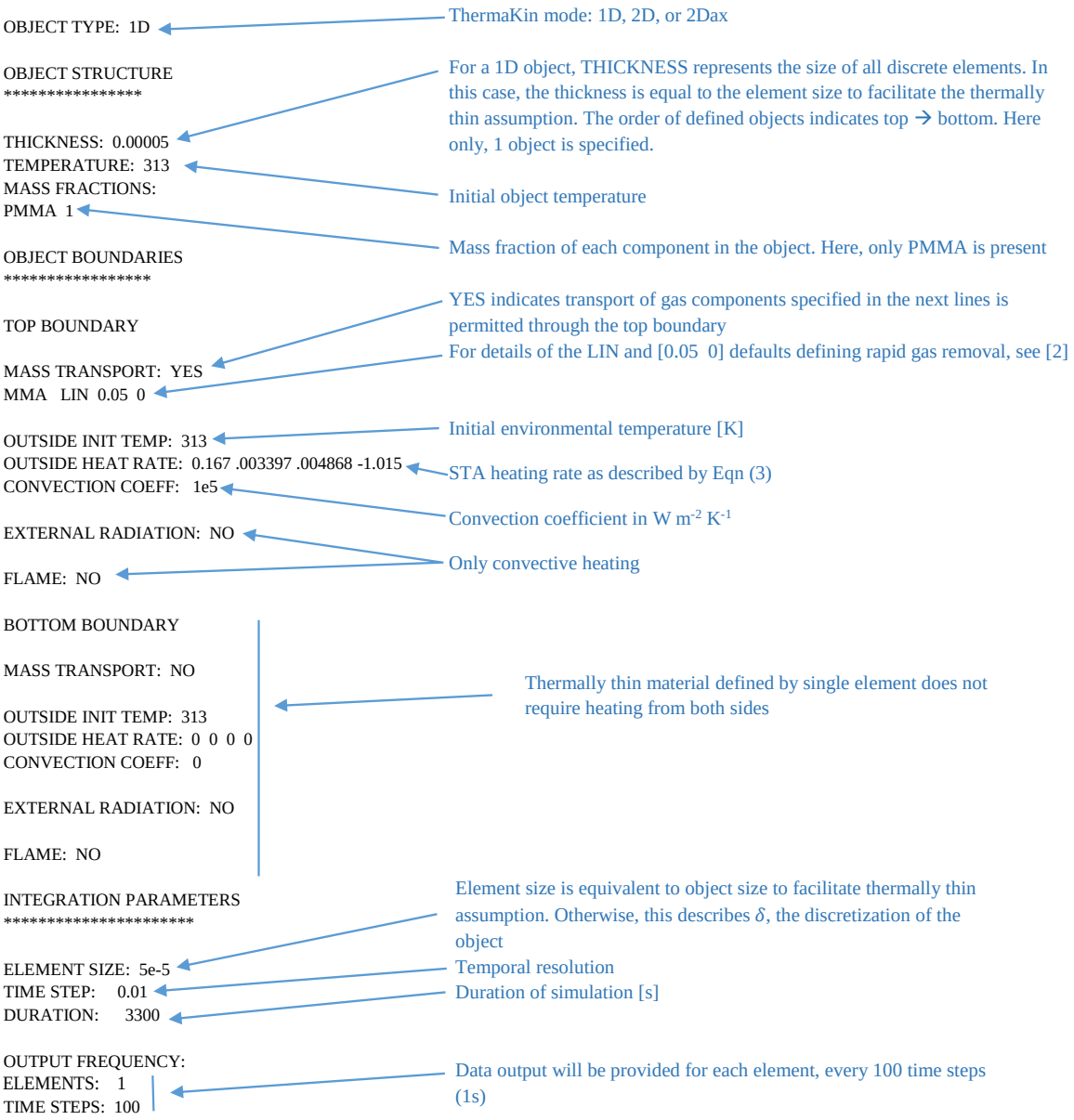

Bibliography

[1] C. Lautenberger, C. Fernandez-Pello, Generalized pyrolysis model for combustible solids, Fire Saf. J. 44 (2009) 819–839. doi:10.1016/j.firesaf.2009.03.011.

[2] S.I. Stoliarov, R.E. Lyon, Thermo-kinetic model of burning for pyrolyzing materials, in: Fire Saf. Sci., 2008. doi:10.3801/IAFSS.FSS.9-1141.

[3] K. McGrattan, S. Hostikka, R. McDermott, J. Floyd, M. Vanella, Sixth Edition Fire Dynamics Simulator Technical Reference Guide Volume 1 : Mathematical Model 6.3, 1 (2015).

[4] C. Lautenberger, C. Fernandez-Pello, Optimization algorithms for material pyrolysis property estimation, in: Fire Saf. Sci., 2011. doi:10.3801/IAFSS.FSS.10-751.

[5] D.M. Marquis, E. Guillaume, A. Camillo, T. Rogaume, F. Richard, Existence and uniqueness of solutions of a differential equation system modeling the thermal decomposition of polymer materials, Combust. Flame. 160 (2013) 818–829. doi:10.1016/J.COMBUSTFLAME.2012.12.008.

[6] T. Rogaume, Kinetics and mechanisms of thermal degradation of pmma by non-isothermal thermogravimety Kinetics and Mechanisms of the Thermal Degradation of Polymethyl Methacrylate by TGA / FTIR Analysis, (2016).

[7] T. Fateh, F. Richard, T. Rogaume, P. Joseph, Experimental and modelling studies on the kinetics and mechanisms of thermal degradation of polymethyl

methacrylate in nitrogen and air, J. Anal. Appl. Pyrolysis. 120 (2016) 423–433. doi:10.1016/J.JAAP.2016.06.014.

[8] E. Kim, N. Dembsey, Engineering Guide for Estimating Material Pyrolysis Properties for Fire Modeling, Proj. Final Rep. (2012) 382.

[9] ASTM International, E1354-17 Standard Test Method for Heat and Visible Smoke Release Rates for Materials and Products Using an Oxygen Consumption Calorimeter, (2017). doi:https://doi.org/10.1520/E1354-17.

[10] ASTM International, E2058-19 Standard Test Methods for Measurement of Material Flammability Using a Fire Propagation Apparatus (FPA), (2019). https://doi.org/10.1520/E2058-19.

[11] Z. Ghorbani, R. Webster, M. Lázaro, A. Trouvé, Limitations in the predictive capability of pyrolysis models based on a calibrated semi-empirical approach, Fire Saf. J. 61 (2013) 274–288. doi:10.1016/J.FIRESAF.2013.09.007.

[12] S.I. Stoliarov, J. Li, Parameterization and Validation of Pyrolysis Models for Polymeric Materials, Fire Technol. 52 (2016) 79–91. doi:10.1007/s10694-015-0490-1.

[13] J.D. Swann, Y. Ding, M.B. McKinnon, S.I. Stoliarov, Controlled atmosphere pyrolysis apparatus II (CAPA II): A new tool for analysis of pyrolysis of charring and intumescent polymers, Fire Saf. J. 91 (2017) 130–139. doi:10.1016/J.FIRESAF.2017.03.038.

[14] C. Darwin, R.L. Livezey, On the Origin of Species by Means of Natural Selection, Am. Midl. Nat. (1953). doi:10.2307/2485224.

[15] A. Matala, S. Hostikka, J. Mangs, Estimation of pyrolysis model parameters for solid materials using thermogravimetric data, in: Fire Saf. Sci., 2008. doi:10.3801/IAFSS.FSS.9-1213.

[16] G. Rein, C. Lautenberger, A.C. Fernandez-Pello, J.L. Torero, D.L. Urban, Application of genetic algorithms and thermogravimetry to determine the kinetics of polyurethane foam in smoldering combustion, Combust. Flame. 146 (2006) 95–108. doi:10.1016/J.COMBUSTFLAME.2006.04.013.

[17] C. Lautenberger, G. Rein, C. Fernandez-Pello, The application of a genetic algorithm to estimate material properties for fire modeling from bench-scale fire test data, Fire Saf. J. 41 (2006) 204–214. doi:10.1016/J.FIRESAF.2005.12.004.

[18] R. Webster, PYROLYSIS MODEL PARAMETER OPTIMIZATION USING A CUSTOMIZED STOCHASTIC HILL-CLIMBER ALGORITHM AND BENCH SCALE FIRE TEST DATA, Master's Thesis, University of Maryland, 2009.

[19] M. Chaos, M.M. Khan, N. Krishnamoorthy, J.L. de Ris, S.B. Dorofeev, Evaluation of optimization schemes and determination of solid fuel properties for CFD fire models using bench-scale pyrolysis tests, Proc. Combust. Inst. 33 (2011) 2599–2606. doi:10.1016/J.PROCI.2010.07.018.

[20] M. Chaos, M.M. Khan, S.B. Dorofeev, Pyrolysis of corrugated cardboard in inert and oxidative environments, Proc. Combust. Inst. (2013). doi:10.1016/j.proci.2012.06.031.

[21] C.G. McCoy, J.L. Tilles, S.I. Stoliarov, Empirical Model of flame heat feedback for simulation of cone calorimetry, Fire Saf. J. 103 (2019) 38–48. doi:10.1016/j.firesaf.2018.11.006.

[22] J. Li, S.I. Stoliarov, Measurement of kinetics and thermodynamics of the thermal degradation for non-charring polymers, Combust. Flame. 160 (2013) 1287–1297. doi:10.1016/J.COMBUSTFLAME.2013.02.012.

[23] J. Li, S.I. Stoliarov, Measurement of kinetics and thermodynamics of the thermal degradation for charring polymers, Polym. Degrad. Stab. 106 (2014) 2–15. doi:10.1016/j.polymdegradstab.2013.09.022.

[24] M.B. McKinnon, S.I. Stoliarov, Pyrolysis model development for a multilayer floor covering, Materials (Basel). (2015). doi:10.3390/ma8095295.

[25] J. Li, J. Gong, S.I. Stoliarov, Gasification experiments for pyrolysis model parameterization and validation, Int. J. Heat Mass Transf. 77 (2014) 738–744. doi:10.1016/j.ijheatmasstransfer.2014.06.003.

[26] J. Li, J. Gong, S.I. Stoliarov, Development of pyrolysis models for charring polymers, Polym. Degrad. Stab. (2015). doi:10.1016/j.polymdegradstab.2015.03.003.

[27] Y. Ding, J.D. Swann, Q. Sun, S.I. Stoliarov, R.H. Kraemer, Development of a pyrolysis model for glass fiber reinforced polyamide 66 blended with red phosphorus: Relationship between flammability behavior and material composition, Compos. Part B Eng. 176 (2019) 107–263. doi:10.1016/J.COMPOSITESB.2019.107263.

[28] M.R. Semmes, X. Liu, M.B. Mckinnon, S.I. Stoliarov, A. Witkowski, A model for oxidative pyrolysis of corrugated cardboard, in: Fire Saf. Sci., 2014. doi:10.3801/IAFSS.FSS.11-111.

[29] S.I. Stoliarov, N. Safronava, R.E. Lyon, The effect of variation in polymer properties on the rate of burning, Fire Mater. (2009). doi:10.1002/fam.1003.

[30] G.T. Linteris, Numerical simulations of polymer pyrolysis rate: Effect of property variations, Fire Mater. (2011). doi:10.1002/fam.1066.

[31] N. Bal, Uncertainty and complexity in pyrolysis modelling, (Ph.D. Dissertation), The University of Edinburgh, 2012.

[32] S.L. Madorsky, Thermal Degradation of Organic Polymers, Intersci. Publ. (1964).

[33] S.I. Stoliarov, S. Crowley, R.E. Lyon, G.T. Linteris, Prediction of the burning rates of non-charring polymers, Combust. Flame. 156 (2009) 1068–1083. doi:10.1016/J.COMBUSTFLAME.2008.11.010.

[34] Y. Pizzo, J.L. Consalvi, P. Querre, M. Coutin, L. Audouin, B. Porterie, J.L. Torero, Experimental observations on the steady-state burning rate of a vertically oriented PMMA slab, Combust. Flame. 152 (2008) 451–460. doi:10.1016/J.COMBUSTFLAME.2007.06.020.

[35] B.T. Rhodes, J.G. Quintiere, Burning rate and flame heat flux for PMMA in a cone calorimeter, Fire Saf. J. 26 (1996) 221–240. doi:10.1016/S0379-7112(96)00025-2.

[36] I.T. Leventon, K.T. Korver, S.I. Stoliarov, A generalized model of flame to

surface heat feedback for laminar wall flames, Combust. Flame. 179 (2017) 338–353. doi:10.1016/J.COMBUSTFLAME.2017.02.007.

[37] O. Korobeinichev, M. Gonchikzhapov, A. Tereshchenko, I. Gerasimov, A. Shmakov, A. Paletsky, A. Karpov, An experimental study of horizontal flame spread over PMMA surface in still air, Combust. Flame. 188 (2018) 388–398. doi:10.1016/j.combustflame.2017.10.008.

[38] J. Zhang, T.J. Shields, G.W.H. Silcock, Effect of Melting Behaviour on Upward Flame Spread of Thermoplastics, Fire Mater. 21 (1997) 1–6. doi:10.1002/(sici)1099-1018(199701)21:1<1::aid-fam583>3.3.co;2-g.

[39] A. Fernandez-Pello, F.A. Williams, LAMINAR FLAME SPREAD OVER PMMA SURFACES, Symp. Combust. (1975). doi:10.1016/S0082-0784(75)80299-2.

[40] O.P. Korobeinichev, A.I. Karpov, A.A. Bolkisev, A.A. Shaklein, M.B. Gonchikzhapov, A.A. Paletsky, A.G. Tereshchenko, A.G. Shmakov, I.E. Gerasimov, A. Kumar, An experimental and numerical study of thermal and chemical structure of downward flame spread over PMMA surface in still air, Proc. Combust. Inst. 37 (2019) 4017–4024. doi:10.1016/j.proci.2018.06.005.

[41] I.T. Leventon, J. Li, S.I. Stoliarov, A flame spread simulation based on a comprehensive solid pyrolysis model coupled with a detailed empirical flame structure representation, Combust. Flame. 162 (2015) 3884–3895. doi:10.1016/J.COMBUSTFLAME.2015.07.025.

[42] S.I. Stoliarov, P.R. Westmoreland, M.R. Nyden, G.P. Forney, A reactive

molecular dynamics model of thermal decomposition in polymers: I. Poly(methyl methacrylate), Polymer (Guildf). 44 (2002) 883–894. doi:10.1016/S0032-3861(02)00761-9.

[43] T. Kashiwagi, A. Inabi, A. Hamins, Behavior of primary radicals during thermal degradation of poly(methyl methacrylate), Polym. Degrad. Stab. 26 (1989) 161–184. doi:10.1016/0141-3910(89)90007-4.

[44] J.E.J. Staggs, Population balance models for the thermal degradation of PMMA, Polymer (Guildf). 48 (2007) 3868–3876. doi:10.1016/j.polymer.2007.04.075.

[45] T. Kashiwagi, A. Inaba, J.E. Brown, Differences in Pmma Degradation Characteristics and Their Effects on Its Fire Properties., (1986) 483–493.

[46] M. Günther, A. Lorenzetti, B. Schartel, Fire phenomena of rigid polyurethane foams, Polymers (Basel). 10 (2018). doi:10.3390/polym10101166.

[47] J.L. Torero, GREN FELL TOWER : PHASE 1 REPORT, (2018) 1–181.

[48] R.E. Lyon, N. Safronava, J. Senese, S.I. Stoliarov, Thermokinetic model of sample response in nonisothermal analysis, Thermochim. Acta. 545 (2012) 82–89. doi:10.1016/J.TCA.2012.06.034.

[49] ASTM International, ASTM D7309-19 Standard Test Method for Determining Flammability Characteristics of Plastics and Other Solid Materials Using Microscale Combustion Calorimetry, (n.d.). https://doi.org/10.1520/D7309-19.

[50] R.E. Lyon, R.N. Walters, S.I. Stoliarov, N. Safronava, Principles and practice of microscale combustion calorimetry, Fed. Aviat. Adm. Atl. City Airport, NJ

8405. (2013) 1–80. doi:DOT/FAA/TC-12/53, R1.

[51] G. Linteris, M. Zammarano, B. Wilthan, L. Hanssen, Absorption and reflection of infrared radiation by polymers in fire-like environments, Fire Mater. (2012). doi:10.1002/fam.1113.

[52] D. Chaudhari, Pending Ph. D. Dissertation, Expected 2020, University of Maryland, Department of Fire Protection Engineering, n.d.

[53] J.D. Swann, Y. Ding, S.I. Stoliarov, Characterization of pyrolysis and combustion of rigid poly(vinyl chloride) using two-dimensional modeling, Int. J. Heat Mass Transf. (2019). doi:10.1016/j.ijheatmasstransfer.2018.12.011.

[54] J.D. Swann, A COMPREHENSIVE CHARACTERIZATION OF PYROLYSIS AND COMBUSTION OF INTUMESCENT AND CHARRING POLYMERS USING TWO-DIMENSIONAL MODELING: A RELATIONSHIP BETWEEN THERMAL TRANSPORT AND THE PHYSICAL STRUCTURE OF THE INTUMESCENT CHAR, Ph. D. Dissertation, University of Maryland, 2019.

[55] F.P. Incropera, D.P. DeWitt, T.L. Bergman, A.S. Lavine, Fundamentals of Heat and Mass Transfer 6th Edition, 2007. doi:10.1016/j.applthermaleng.2011.03.022.

[56] R.E. Lyon, R.N. Walters, S.I. Stoliarov, A thermal analysis method for measuring polymer flammability, J. ASTM Int. 3 (2006) 1–18. doi:10.1520/JAI13895.

[57] T. Nyazika, M. Jimenez, F. Samyn, S. Bourbigot, Pyrolysis modeling,

sensitivity analysis, and optimization techniques for combustible materials: A review, J. Fire Sci. 37 (2019) 377–433. doi:10.1177/0734904119852740.

[58] K. McGrattan, S. Hostikka, R. McDermott, J. Floyd, M. Vanella, Fire Dynamics Simulator Technical Reference Guide Volume 2 : Verification, 1018–2 (2018) 1–147. doi:http://dx.doi.org/10.6028/NIST.SP.1018-1.

[59] NOAA, Cameo Chemicals, (n.d.), METHYL METHACRYALTE MONOMER. https://cameochemicals.noaa.gov/chemical/7108.

[60] P.J. Linstrom, W.G. Mallard, NIST Chemistry WebBook, NIST Standard Reference Database Number 69, (2018). doi:10.18434/T4D303.

[61] T. Steinhaus, EVALUATION OF THE THERMOPHYSICAL PROPERTIES OF POLY(METHYL METHACRYLATE): A REFERENCE MATERIAL FOR THE DEVELOPMENT OF A FLAMMABILITY TEST FOR MICRO-GRAVITY ENVIRONMENTS, Master's Thesis, University of Maryland, Department of Fire Protection Engineering, 1999. https://www.era.lib.ed.ac.uk/handle/1842/2831.

[62] Y.C. Wang, A. Foster, Experimental and numerical study of temperature developments in PIR core sandwich panels with joint, Fire Saf. J. 90 (2017) 1–14. doi:10.1016/J.FIRESAF.2017.03.003.